nature research

https://doi.org/10.1038/s41563-020-0774-9

Supplementary information

Intrinsic quantum confinement in formamidinium lead triiodide perovskite

In the format provided by the authors and unedited

Supplementary Information: Intrinsic quantum confinement in formamidinium lead triiodide perovskite

Adam D. Wright[1], *George Volonakis*[2,3], *Juliane Borchert*[1], *Christopher L. Davies*[1], *Feliciano Giustino*[2,4,5], *Michael B. Johnston*[1] *and Laura M. Herz*[1]*

Email: laura.herz@physics.ox.ac.uk

[1]Department of Physics, University of Oxford, Clarendon Laboratory, Parks Road, Oxford OX1 3PU, United Kingdom

[2]Department of Materials, University of Oxford, Parks Road, Oxford OX1 3PH, United Kingdom

[3] Univ Rennes, ENSCR, INSA Rennes, CNRS, ISCR (Institut des Sciences Chimiques de Rennes), UMR 6226, Rennes F-35000, France

[4] Oden Institute for Computational Engineering and Sciences, The University of Texas at Austin, Austin, Texas 78712, USA

[5] Department of Physics, The University of Texas at Austin, Austin, Texas 78712, USA

Contents

Supplementary Note 1: Film Deposition & X-ray Diffraction

The $FAPbI_3$ thin films were co-evaporated in a modified Kurt J. Lesker Mini Spectros evaporator, on *z*-cut quartz substrates as reported previously [1,2]. The precursors were PbI_2 beads with 99.999% purity from Alfa Aesar and FAI from Greatcell Solar Materials. These precursors were placed in separate alumina crucibles and heated until they evaporated. The samples were mounted above and rotated to enable uniform deposition. The same rates and setting were used for all films with thicknesses above 100 nm, with only the length of the evaporation altered to vary the thickness of the film. When these same settings were used for the very thin films (10 nm and 35 nm film thickness), significant amounts of PbI_2 were evident. To avoid this secondary phase, the FAI rate was increased for these two thinnest samples to decrease the amount of PbI_2 in the thin film.

After the deposition, all $FAPbI_3$ thin films were annealed (except for one 433 nm film) at 170 °C for 1 min to ensure that they were in the correct perovskite α-$FAPbI_3$ phase. To confirm this, their X-ray diffraction (XRD) patterns were measured in air using a Panalytical X'pert powder diffractometer with a copper X-ray source, and are shown in Supplementary Figure 1. From these, it is evident that all the films were in the perovskite α-$FAPbI_3$ phase (as confirmed by visual inspection) to within the detection limit of the system, which is usually around 2-3 wt% for XRD [3]. Supplementary Figure 2 depicts XRD patterns which show the conversion of the vast majority of δ-phase into α-phase during annealing. Because of experimental limitations specific to the XRD apparatus (but not the FTIR), it was not possible to measure the XRD pattern of the 10 nm sample without water infiltration into the perovskite [4] resulting in its conversion to the hexagonal non-perovskite δ-phase due to exposure to humidity [2] during transport to, and measurement in, the x-ray diffractometer.

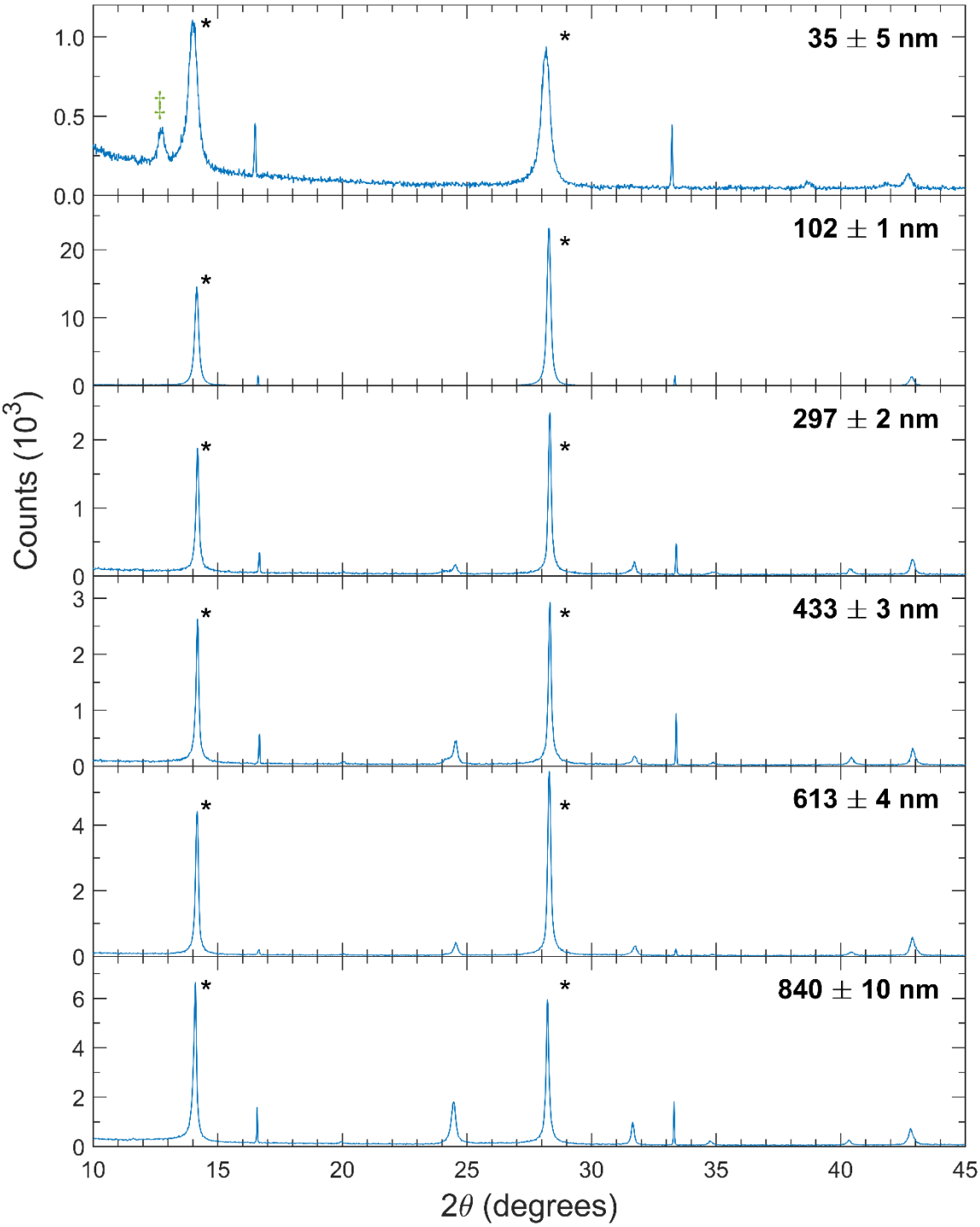

Supplementary Figure 1 | X-ray diffraction patterns for the $FAPbI_3$ films. Thicknesses are indicated in the top-right corner of each panel. Black asterisks (*) indicate prominent peaks corresponding to the perovskite α-$FAPbI_3$ phase. The green double dagger (‡) marks the PbI_2 peak [5]. If present, the non-perovskite δ-$FAPbI_3$ phase would have been indicated by a peak at $2\theta \approx 12°$ [2]. The XRD patterns were analysed with the Cu Kα line.

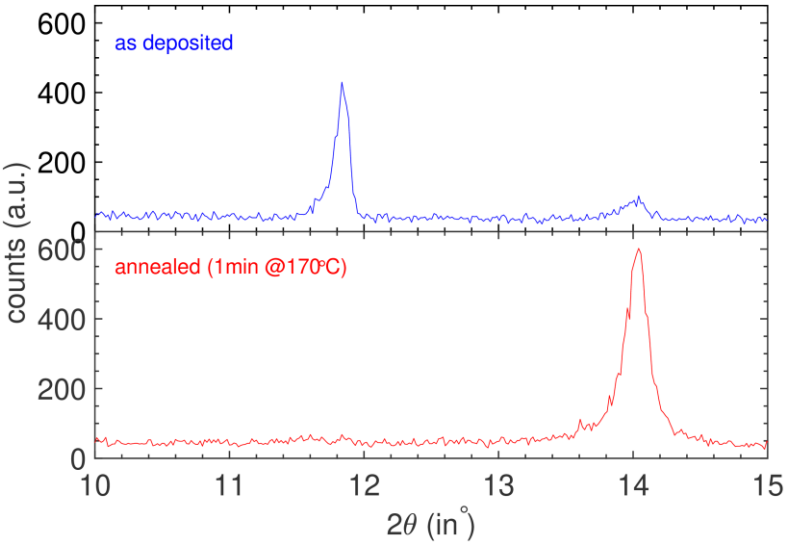

Supplementary Figure 2 | X-ray diffraction patterns before and after annealing. The delta phase peak at 12° is prominently visible in the sample before annealing, but after annealing the alpha phase peak at 14° is dominant. These data are from a 370 nm-thick $FAPbI_3$ film which belonged to a different batch from the films discussed in the rest of this study, but was fabricated in an analogous manner [2].

Supplementary Note 2: Current-Voltage (J-V) Curve of Device

A solar cell based on an evaporated $FAPbI_3$ film was fabricated using a standard architecture. The substrate was fluoride-doped tin oxide (FTO) coated glass. It was cleaned by sonication in acetone and isopropanol and cleaning with an oxygen plasma. The fullerene C_{60} was evaporated onto the clean FTO substrates. C_{60} with a purity of 99.9% from Acros Organics was evaporated at 350 °C. The perovskite layer was co-evaporated onto this as described above. Next the hole extraction material 2,2',7,7'-Tetrakis-(N,N-di-4-methoxyphenylamino)-9,9'-spirobifluorene (Spiro-OMeTAD) from Lumtec was spin-coated on top. Spiro-OMeTAD was doped with Lithium bis(trifluoromethanesulfonyl)imide (LiTFSI) and 4-tert-Butylpyridine (tBP) and the solution spin coated at 2000 rpm for 45 s. Finally, 100nm of silver were evaporated to contact the solar cells. The size of the evaporated metal contacts was 0.0919 cm^2.

The current-voltage (J–V) measurements, shown in Supplementary Figure 3, were carried out on the device under illumination with an ABET class AAB sun 2000 simulator. The scan speed was 0.38 V s^{-1}. The short-circuit current density (J_{SC}) was 22 mA cm^{-2}, which is 80 % of the maximum possible J_{SC} of 27.63 mA cm^{-2} for a 1.54 eV bandgap (see Fig. 2a of the main text) material under AM1.5 illumination [6].

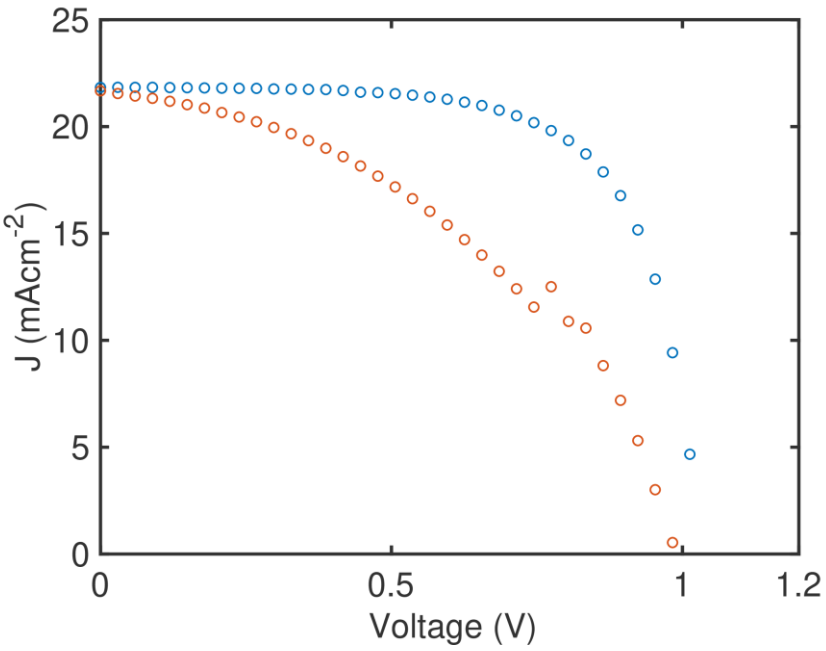

Supplementary Figure 3 | Current-voltage (J-V) curve of the $FAPbI_3$ photovoltaic device. The forward sweep is plotted in red and the reverse sweep in blue. The short-circuit current density (J_{SC}) was 22 mA cm^{-2}. Data on comparable devices from the same batch were previously reported by Borchert *et al*. [2].

Supplementary Note 3: Absorption Measurements and Ruling-out of Optical or Measurement Artefacts

Absorption measurements techniques

Absorption coefficient spectra for six $FAPbI_3$ films of thicknesses ranging from 35 nm to 840 nm are shown in Supplementary Figure 5, for temperatures between 4 K and 295 K. The absorption coefficient (α) was obtained from the transmittance (T) and reflectance (R) spectra (Supplementary Figure 4) by the relationship

$$\alpha = -\frac{1}{d}\ln\left(\frac{T}{1-R}\right)$$

where d is the thickness of the film, measured using a DEKTAK profiler or atomic force microscope, as described in Supplementary Note 12. For absorption data shown in all figures but Supplementary Figure 6, T and R were measured using a Fourier transform infrared (FTIR) spectrometer (Bruker Vertex 80v), configured with a tungsten halogen lamp illumination source, a CaF_2 beamsplitter and a silicon detector. The samples were mounted in a gas-exchange helium cryostat (Oxford Instruments, OptistatCF2) and heated over temperatures ranging between 4 to 295 K in increments of between 5 and 10 K.

To corroborate the spectra measured using the FTIR, the room temperature absorption spectra of five of the $FAPbI_3$ films were also measured with a dispersive spectrophotometer (Perkin-Elmer Lambda 1050), as shown in Supplementary Figure 6.

Ruling out optical interference effects as origin of peak features

We first took several steps to ensure that the observed peak-like features superimposed on the otherwise relatively uniform absorption profile did not arise from a measurement or optical artefact. To corroborate that these features were not related to the measurement technique (FTIR spectroscopy), we also determined absorption spectra for these films at room temperature using a dispersive spectrometer (UV-VIS spectrophotometer), which confirmed the presence of the peak features (Supplementary Figure 6). In addition, it is evident that these oscillations are not caused by optical interference effects deriving from the films' interfaces. Such Fabry-Pérot oscillations are of course present in the reflectance spectra, demonstrating the uniform thickness and optical flatness of the film [7] (see for example the inset to Fig. 1a of the main manuscript) but display a larger energy spacing than the oscillations observed in the absorption spectra, which were present in both the transmittance and reflectance spectra (see Supplementary Figure 4). In addition, the peak structures we observed in the absorption coefficient spectra are not equally spaced in wavelength, and are largely invariant with film thickness (see Supplementary Figure 5), ruling out optical interference effects as their origin.

Showing that confinement features are only present in the perovskite phases of $FAPbI_3$

In addition, we confirmed that the observed features are clearly attributable to the semiconducting perovskite phases of $FAPbI_3$. We note that following initial casting, $FAPbI_3$ films tend to crystallise as the thermodynamically stable yellow non-perovskite δ-phase at room temperature [8], which is not photoactive and hinders electron transport [9], though some presence is not entirely negative [10]. The desirable polymorph is the black, perovskite α-phase, obtained by annealing films above 150°C [11,12]. Return to room temperature leaves the film initially in the black perovskite α-phase, although this eventually converts back slowly to the yellow δ-phase under ambient conditions [13]. $FAPbI_3$ further boasts three structurally different perovskite phases over different temperature intervals: cooling from the α-phase results in transitions to the β-phase near 285K, followed by the γ-phase below ≈140K. We found that no peaks are apparent in the temperature-dependent absorption spectra of $FAPbI_3$ films that had not been annealed and had thus remained in the original δ-phase (Supplementary Figure 7), indicating that the features are only associated with the perovskite phases of $FAPbI_3$, and again ruling out optical artefacts resulting from thin-film interference effects. In addition, we found that a $MAPbI_3$ film measured under identical conditions to a comparable $FAPbI_3$ film did not exhibit absorption oscillations either (Supplementary Figure 8). Therefore, the modulations are clearly intrinsic to the semiconducting perovskite phases of $FAPbI_3$.

Ruling out other physical effects as origin of peak features

Having established that only the semiconducting perovskite phases of $FAPbI_3$ sustain such peak-like features, we can rule out some other physical explanations (besides optical interference) that have been applied to above-bandgap absorption features. Neither are there transitions between higher-lying bands [14] to explain such features, nor can they be Franz-Keldysh oscillations since they are neither evenly spaced, nor decreasing in amplitude with increasing energy [15]. Rather, these oscillatory features most closely resemble those observed in quantum confined semiconductors, such as in the spectra of 2D InAs nanolayers [16].

Consistency with previous reports on optical absorption spectra of $FAPbI_3$

If the peak-like features in its absorption are fundamental to $FAPbI_3$, we might expect them to have been inadvertently recorded and thus evident in previously published absorption or transmission spectra. We therefore also carefully examined a range of previously reported absorption spectra of solution-processed $FAPbI_3$ films at room-temperature, and find some clear occurrences of oscillations [17,18] that have not yet received any explanations to date. However, in many cases, oscillations are not immediately discernible [9,10,19–21], and we note that their faint nature at room temperature, together with the larger scattering effects in solution-cast films, means that they appear to be hard to visualize by eye in some cases.

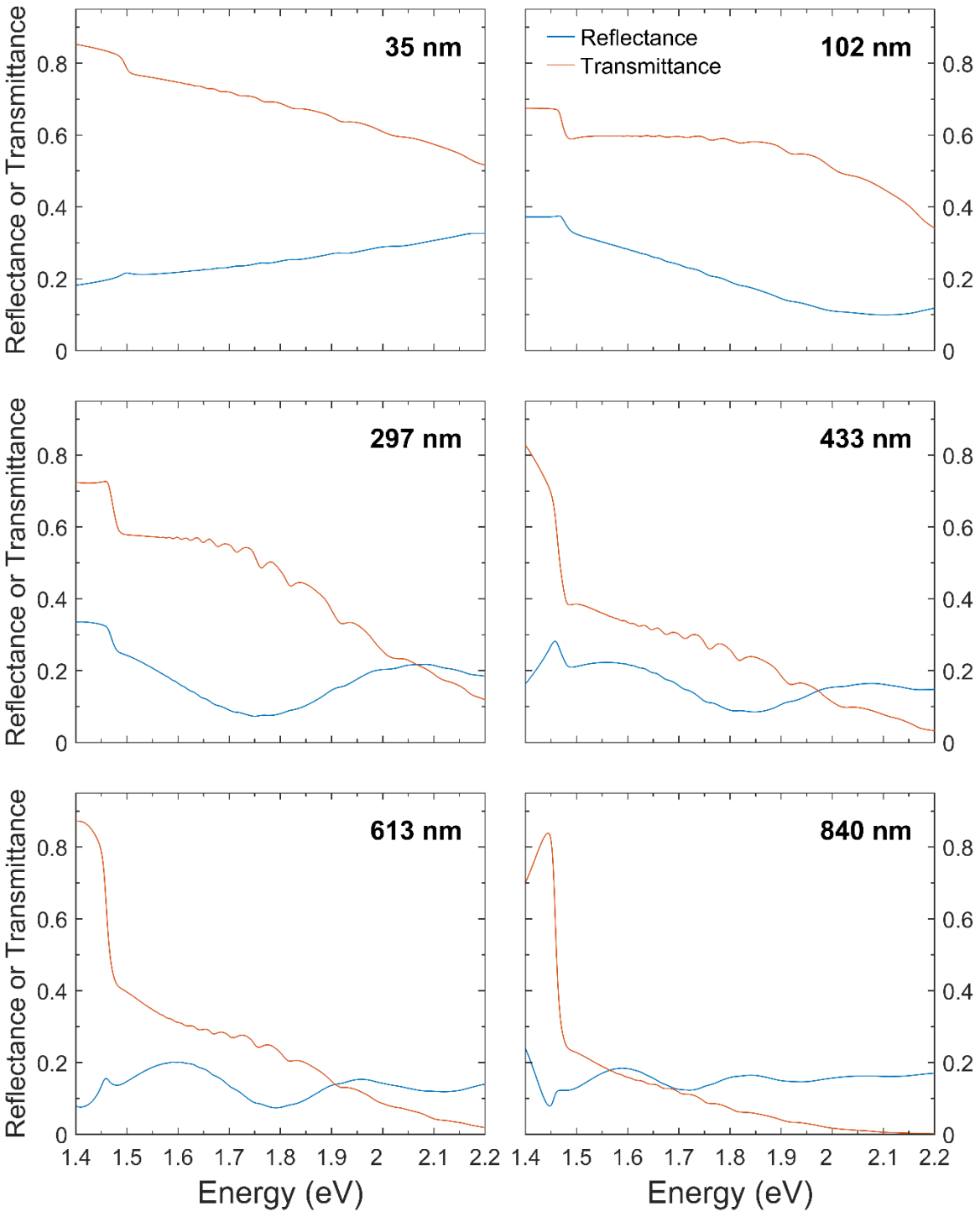

Supplementary Figure 4 | Thickness-dependent reflectance and transmittance spectra of $FAPbI_3$ films at 4 K. The blue lines show the reflectance and the red lines show the transmittance. The onset of Fabry-Perot oscillations can be seen for photon energies below the band gap (~ 1.5 eV), and as expected the Fabry-Perot period shortens with increased film thickness.

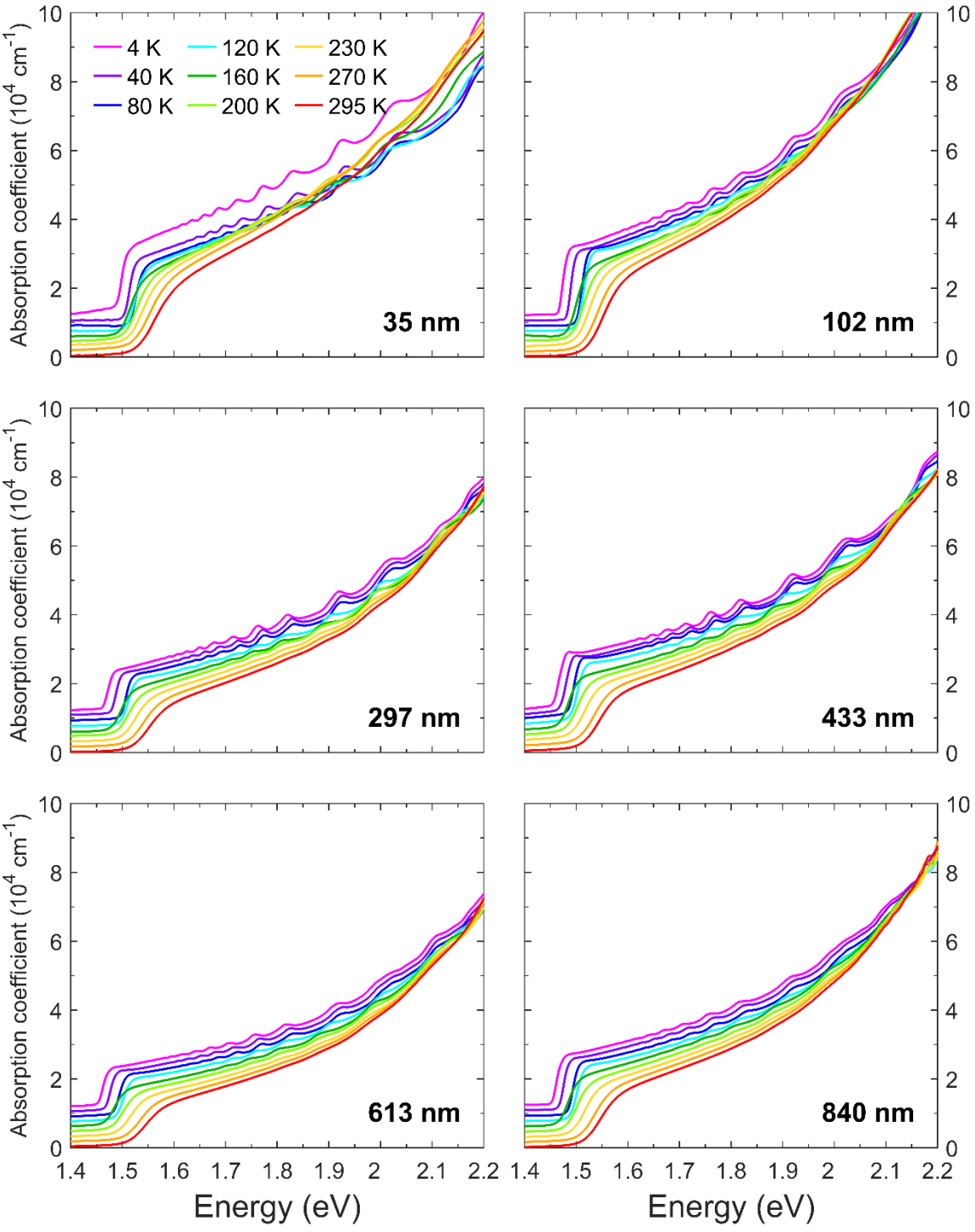

Supplementary Figure 5 | Temperature- and thickness-dependent absorption spectra of $FAPbI_3$. Absorption coefficients of $FAPbI_3$ films are shown at roughly 40 K temperature intervals, from 4 K (magenta) to 295 K (red). The thicknesses of the films are indicated in the bottom-right corner of each panel. For clarity, spectra at successively increasing temperatures are offset vertically by 1.5×10^3 cm^{-1}.

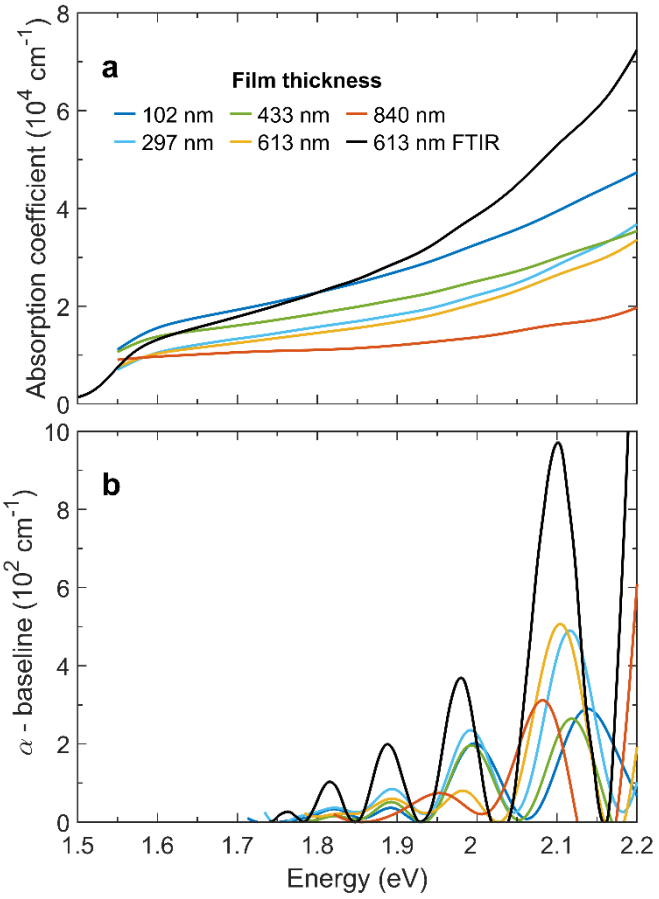

Supplementary Figure 6 | Dispersive spectrometer measurement of absorption coefficient spectra and deduced peak features. a) Absorption coefficients of $FAPbI_3$ films of five thicknesses as measured with a dispersive (grating) spectrometer at room temperature, along with the corresponding data measured on the FTIR spectrometer for the 613 nm film (black), for which the peak features are most prominent. Since the spectral range of the dispersive spectrometer did not extend to wavelengths longer than 800 nm and so did not allow for measurement of the absorption baseline, the data from the dispersive spectrometer were shifted in the y-direction to coincide with the FTIR data at 800 nm (1.55 eV) from the respective samples. In **b)** the peaks extracted from the spectra above are shown, confirming that the features can be observed on two independent measurement systems.

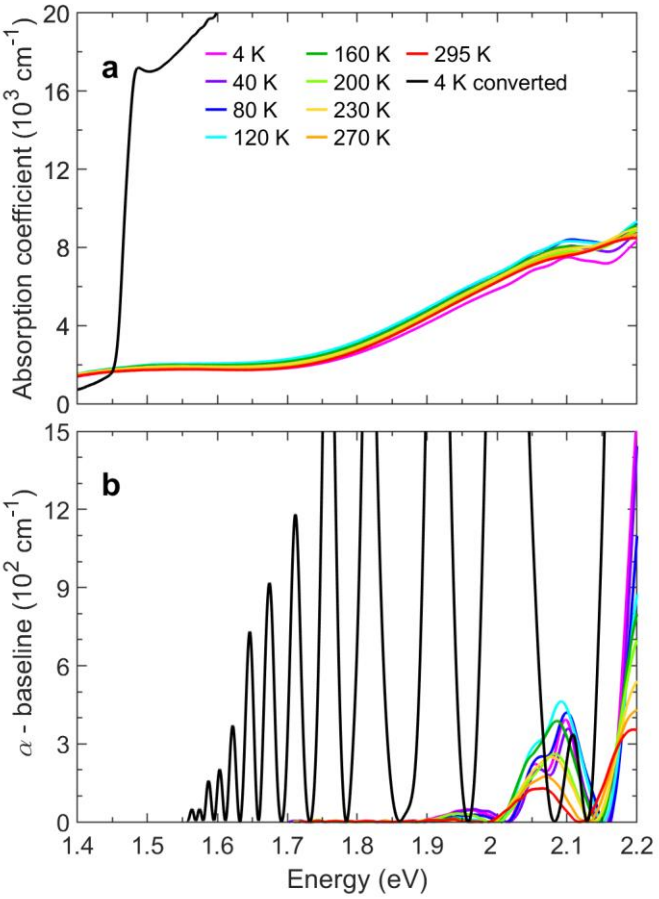

Supplementary Figure 7 | Temperature-dependent absorption coefficient and peak features of unannealed non-perovskite $FAPbI_3$. a) Absorption spectra and **b)** absorption peak features of a 433 nm $FAPbI_3$ film which had not been annealed, at roughly 40 K temperature intervals, from 4 K (magenta) to 295 K (red). The data at 4 K from the annealed 433 nm film in the perovskite phase is shown in black for reference, demonstrating that the same features are not observed in the un-annealed film. The feature above 2 eV may correspond to a high-lying transition, see Supplementary Figure 8.

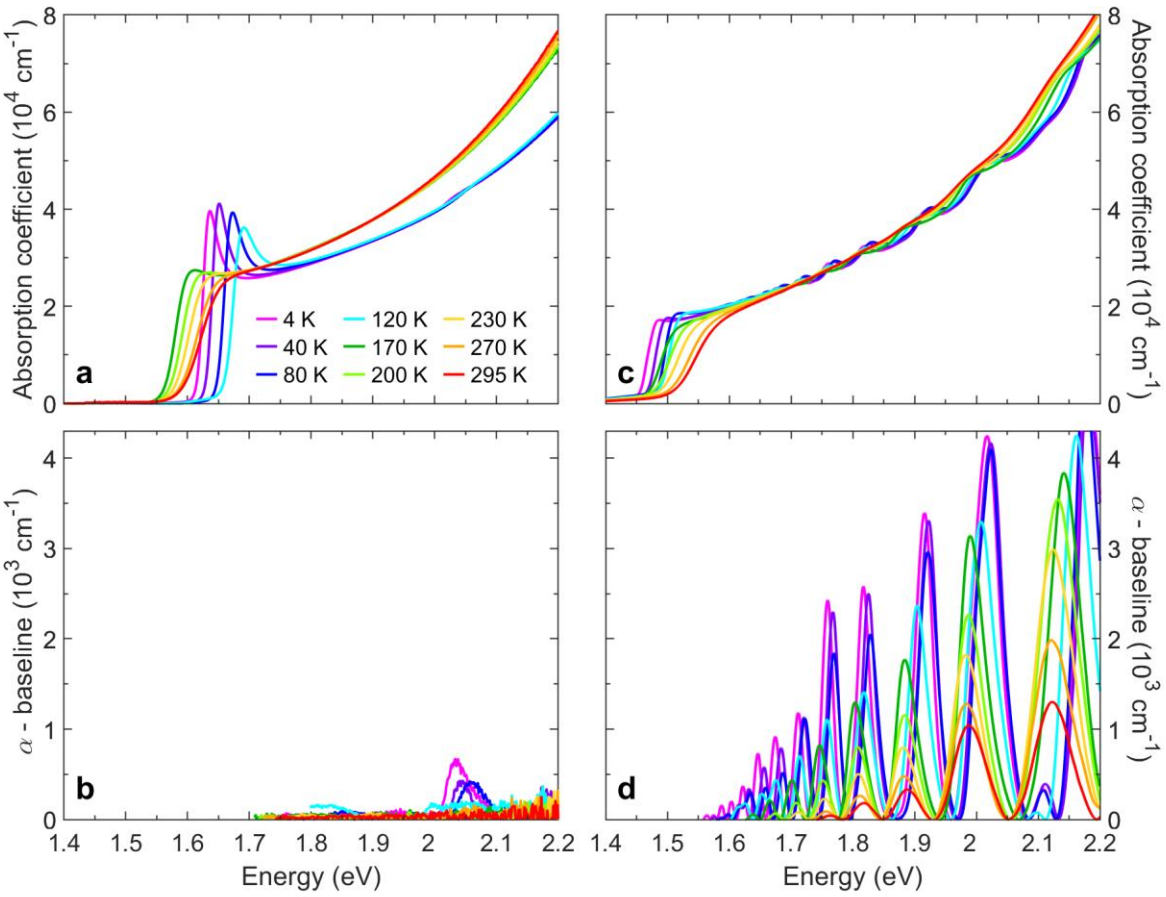

Supplementary Figure 8 | Comparison between absorption spectra of $MAPbI_3$ and $FAPbI_3$. a) Absorption spectra and **b)** absorption peak features for a 435-nm thick $MAPbI_3$ film at roughly 40 K temperature intervals, from 4 K (magenta) to 295 K (red), taken from Davies *et al.* [22] (data used under a Creative Commons Attribution 4.0 International License). **c)** and **d)** show the corresponding data for a 433 nm $FAPbI_3$ film prepared and measured using comparable conditions, demonstrating that the $MAPbI_3$ film does not exhibit the same modulatory features as in $FAPbI_3$. The feature of $MAPbI_3$ above 2 eV may correspond to a high-lying transition.

Supplementary Note 4: Elliott Fitting and Baseline Fitting

Temperature-dependent absorption spectra of $FAPbI_3$ were fitted at the band edge with an expression based on Elliott theory [23], and with a phenomenological fit of our own devising at energies further above the band gap.

Elliott fitting

Elliott's model describes the absorption of a semiconductor near the band edge. We follow the thorough treatment given by Davies *et al.* in applying the model to $MAPbI_3$ [22] and $FAPbI_3$ [1], and thus give only an outline below. The theory expresses the energy-dependent absorption as

$$\alpha(E) = \alpha_{\mathrm{X}}(E) + \alpha_{\mathrm{C}}(E)$$

The bound exciton contribution $\alpha_{\mathrm{X}}(E)$ has the form

$$\alpha_{\mathrm{X}}(E) = \frac{b_0}{E}\sum_{n=1}^{\infty}\frac{4\pi E_{\mathrm{b}}^{3/2}}{n^3}\delta\left(E - \left[E_{\mathrm{g}} - \frac{E_{\mathrm{b}}}{n^2}\right]\right)$$

where b_0 is a constant of proportionality, which incorporates the electric dipole transition matrix element between the valence and conduction band. $\alpha_X(E)$ is formed of the weighted sum of contributions from the exciton states with positive integer quantum number n and energies $E_{\mathrm{g}} - \frac{E_{\mathrm{b}}}{n^2}$, where E_{g} is the band gap energy and E_{b} is the exciton binding energy.

Meanwhile, the contribution from electron-hole continuum states $\alpha_{\mathrm{C}}(E)$ has the form

$$\alpha_{\mathrm{C}}(E) = \frac{b_0}{E}\left[\frac{2\pi\sqrt{\frac{E_{\mathrm{b}}}{E - E_{\mathrm{g}}}}}{1 - \exp\left(-2\pi\sqrt{\frac{E_{\mathrm{b}}}{E - E_{\mathrm{g}}}}\right)}\right]c_0^{-1}\,\mathrm{JDoS}(E)$$

where the joint density of states is given by $\mathrm{JDoS}(E) = c_0\sqrt{E - E_{\mathrm{g}}}$ for $E > E_{\mathrm{g}}$, and 0 otherwise, and the joint density of states constant $c_0 = \frac{1}{(2\pi)^2}\left(\frac{2\mu}{\hbar^2}\right)^{3/2} \times 2$, where μ is the reduced effective mass of the electron-hole system. The term is square brackets is the Coulombic enhancement factor, which increases the absorption from the continuum states above the square-root form of the JDoS for direct-gap semiconductors as a result of the Coulombic attraction between the unbound electrons and holes.

The linear combination of the contributions from the excitonic and continuum states, $\alpha(E)$, is then convolved with a normal distribution, $\mathcal{N}(0, \sigma_T^2)$, which represents broadening due to electron-phonon coupling, disorder and local fluctuations in the stoichiometry of the material. The normal distribution $\mathcal{N}(0, \sigma_T^2)$ has mean 0 and temperature-dependent standard deviation σ_T. Thus, the FWHM of the exciton peak is given by $2\sqrt{2\ln(2)}\sigma_T$. Unlike Davies *et al.* [22], we do not find a log-normal distribution to be also required to describe the broadening.

The final Elliott function is $f_{\mathrm{Elliott}} = \alpha(E) \otimes \mathcal{N}(0, \sigma_T^2)$, where convolution is represented by the symbol $\otimes$. This expression is then fitted to the temperature-dependent experimental absorption coefficient data for a given sample by a least-squares minimisation method, where the three temperature-dependent parameters E_{G}, E_{X} and σ_T are fitted at each temperature. Supplementary Figure 9 shows an example of a final Elliott fit to experimental data.

Baseline fitting

In order to quantify the behaviour of the superimposed peak features, it is necessary to decouple them from the rest of the standard above-bandgap absorption, which is mostly monotonically increasing. Fits based on Elliott's theory [23] are only successful near the band gap for $FAPbI_3$, as the assumptions involved in this theory stop applying with increasing energies [1]. Therefore, we instead apply a phenomenological fit to extract the pertinent peak modulation behaviour from the measured absorption data.

As shown in Supplementary Figure 9, we first applied a smoothing algorithm to the above-bandgap data with a local regression fit using weighted linear least squares and a second-degree polynomial model. This approach yielded a smooth 'central fit' line (shown in green) through the centre of the modulations. Subtracting this line from the experimental data resulted in a purely oscillatory function, whose minima corresponded to the troughs in the features observed in the experimental data, separated from the influence of the underlying rising continuous absorption. By interpolating a piecewise cubic spline between the experimental absorption data at the energies of these minima, we obtained a baseline fit (shown in blue). Subtracting this spline baseline fit from the experimental data produced the peaks shown elsewhere in this study, which were more amenable to quantitative analysis than oscillations around the central fit line.

As a caveat, we however note that while this procedure allows for an essential assessment of the changes in energetic positions of peaks, for example with temperature or sample thickness, it may not adequately account for any underlying, continuous density of states that may also be associated with the quantum confinement. For example, if the confinement were to be solely in one dimension, a two-dimensional step-like density of states reflecting the kinetic energy of charge-carrier motion in the two other (unconfined) directions would be expected (see for example Supplementary Note 10 for the absorption spectrum of a one-dimensional superlattice with two unconfined additional dimensions for carrier motion). Our baseline fits will in this case return a good measure of the onsets of these steps, but will miss much of the underlying two-dimensional density-of-states contribution. If, on the other hand, confinement were to be present in all three dimensions (quantum-dot-like system) a series of discrete (but broadened) peaks would be expected, in which case our methodology reflects the fraction of the absorption caused by the confined domains accurately. Since we cannot tell at this point in how many dimensions the confinement is present, we therefore caution that while the baseline fits capture the energetic positions of electronic confinement levels well, the area under the extracted features may not fully reflect the quantity and fraction of the material that is exhibiting such confinement effects.

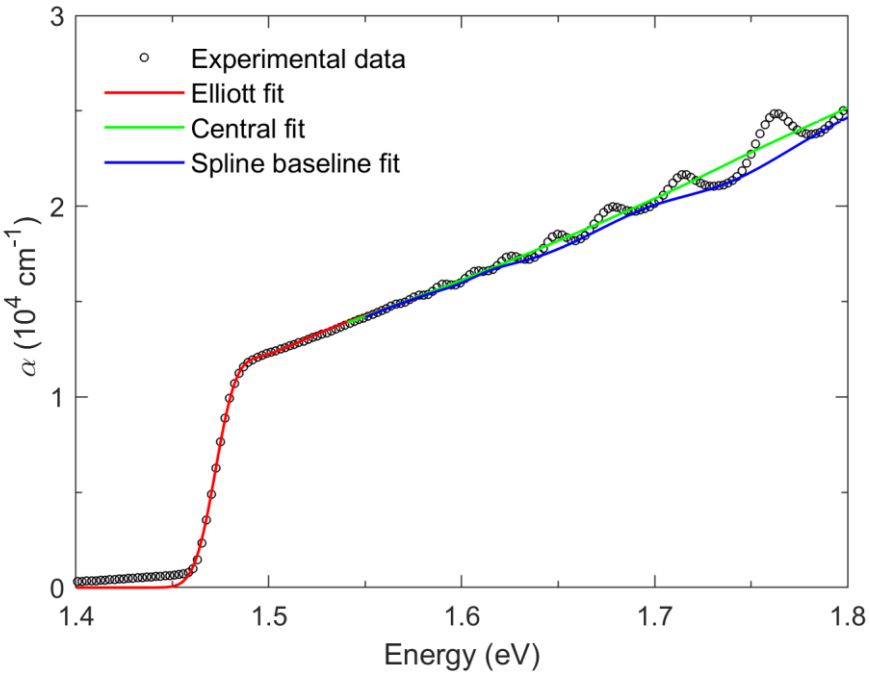

Supplementary Figure 9 | Elliott and baseline fits. Absorption coefficient data (black circles; only every tenth data point is plotted, for clarity) at 4 K for the 297 nm thick sample, fitted at the absorption onset by an Elliott fit (red line) and at higher energies by a phenomenological smoothing function (green line) through the centres of the oscillations. This latter 'central fit' is used to generate the spline baseline fit (blue line) through the troughs of the modulations.

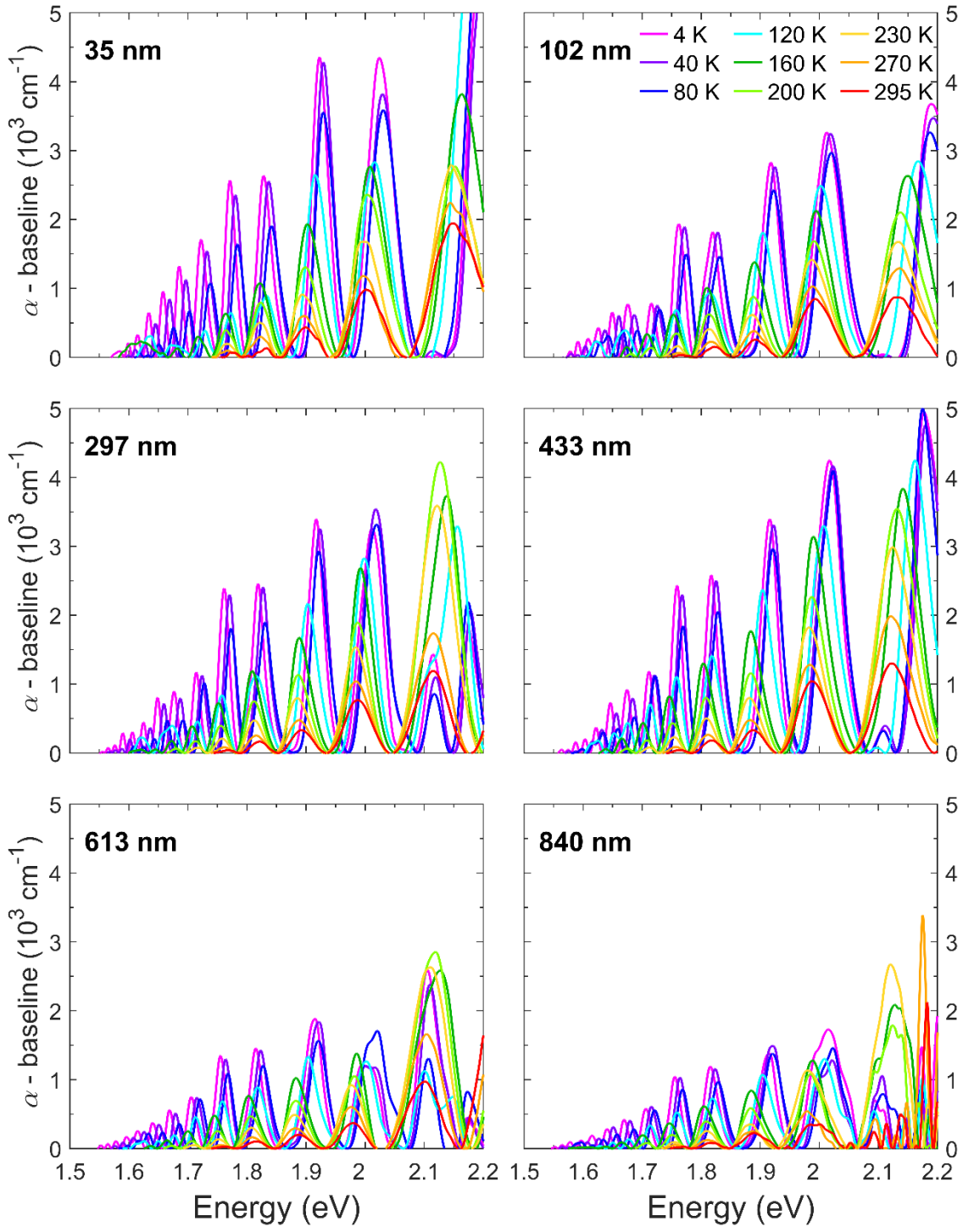

Supplementary Figure 10 | Temperature-dependent oscillatory features. Positions of the peak features, extracted from the absorption spectra of $FAPbI_3$ films are shown at roughly 40 K temperature intervals, from 4 K (magenta) to 295 K (red). The thicknesses of the films are indicated in the top-left corner of each panel.

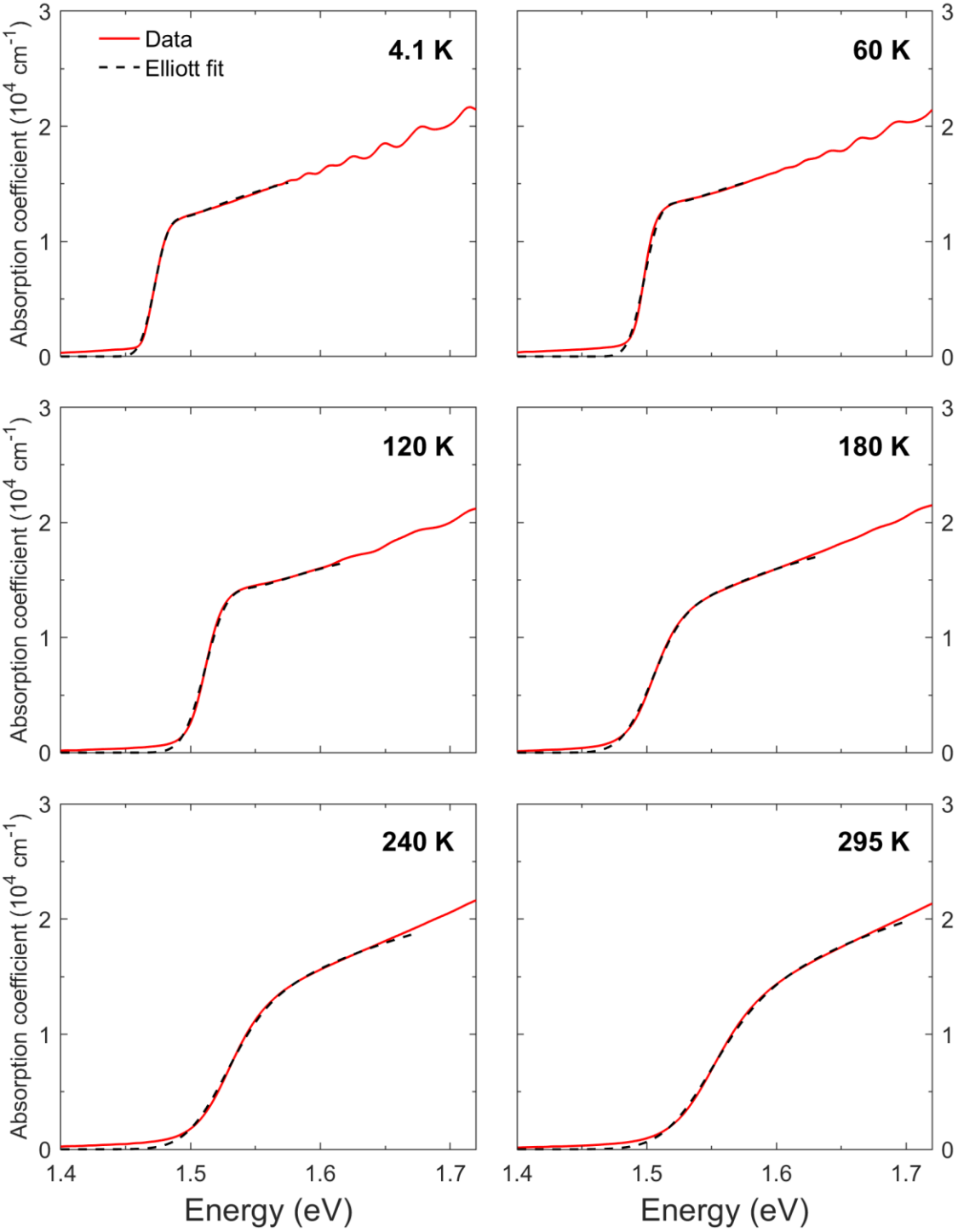

Supplementary Figure 11 | Temperature dependence of Elliott fits. Elliott fits (dotted black lines) to the absorption spectra (red lines) of the 297 nm thick $FAPbI_3$ film, near the band edge. The temperatures of the measurements are indicated in the top-right corner of each panel.

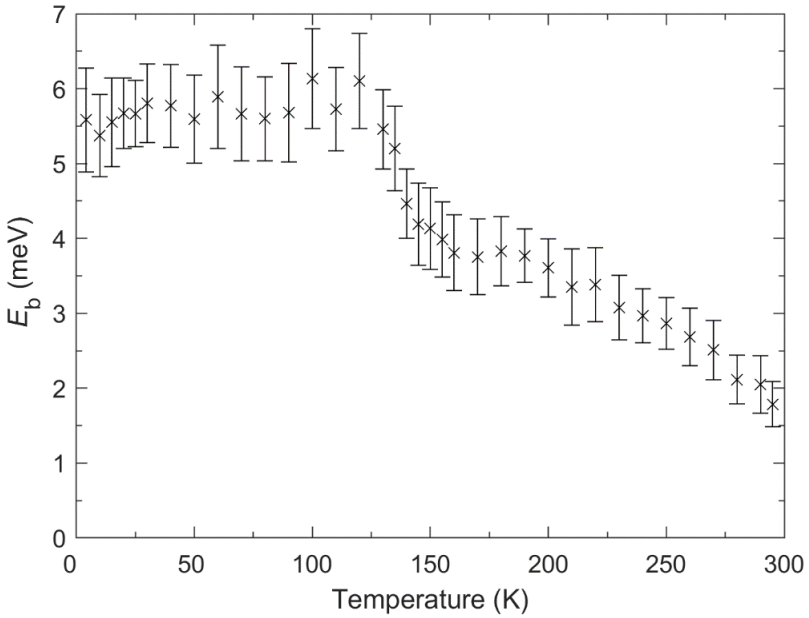

Supplementary Figure 12 | Temperature dependence of the exciton binding energy. Exciton binding energy (E_b) of $FAPbI_3$ extracted from Elliott fits, presented as averages over the parameters extracted from Elliott fits for films of thickness 35, 102, 297, 433, 613 and 840 nm, which showed no trend between E_b and thickness. Error bars show the standard error. The temperature-dependent trend in E_b is consistent with that shown in the study by Davies *et al.* [1], beginning a gradual decrease with temperature starting from around the *γ*-phase to *β*-phase transition. The approximately constant low-temperature value of E_b here is lower than the ~8 meV value obtained by Davies *et al.* [1] using Elliott fitting, but is closer to the 5.3 meV value directly measured from optical pump terahertz probe spectroscopy also reported there.

Supplementary Note 5: Photoluminescence

A 370 nm thick $FAPbI_3$ film was photoexcited by a 398 nm picosecond pulsed diode laser (PicoHarp, LDH-D-C-405M). The resultant PL (Supplementary Figure 13) was collected and coupled into a grating spectrometer (Princeton Instruments, SP-2558), which directed the spectrally dispersed PL onto a silicon iCCD (PI-MAX4, Princeton Instruments). The sample was mounted under vacuum ($P < 10^{-6}$ mbar) in a cold-finger liquid helium cryostat (Oxford Instruments, MicrostatHe). An associated temperature controller (Oxford Instruments, ITC503) monitored the temperature at two sensors mounted on the heat exchanger of the cryostat and the end of the sample holder, respectively; the reading from the latter was taken as the sample temperature.

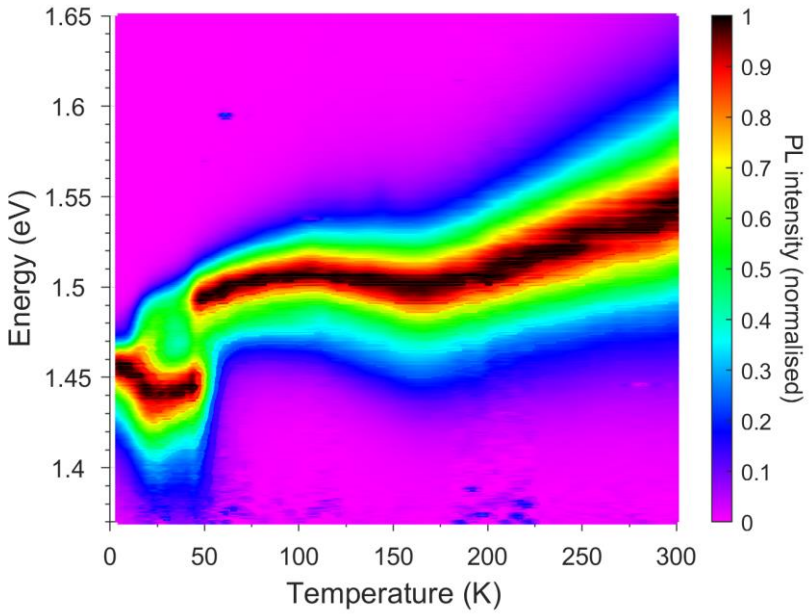

Supplementary Figure 13 | Temperature dependence of photoluminescence (PL). Colour plot of the normalized PL spectra of a 370 nm thick $FAPbI_3$ film at temperatures between 4 and 295 K, under an excitation fluence of 34 nJ cm^{-2}. The temperature-dependence of the peak PL energy is consistent with that of the band gap shown in Fig. 2a of the main text extracted from absorption spectra and with previous reports for solution-processed $FAPbI_3$ [24]. Like $MAPbI_3$, but unlike other notable semiconductors such as GaAs and Si [25], the band gap of $FAPbI_3$ generally blueshifts with increasing temperature [26], apart from the redshift between approximately 100 K and 160 K, which corresponds to the phase transition between the β-phase and the γ-phase[27]. The separate lower-energy peak at temperatures below 50 K is due to band tail states [24]. The prominence of band-edge emission suggests that any charge-carriers generated within quantum confined domains rapidly transfer to the majority bulk states within the time scales of the carrier lifetimes, as would be expected.

Supplementary Note 6: Peak Behaviour

Peak energies

Having separated the peak features from the absorption coefficient data as described in Supplementary Note 4, it was possible to analyse their behaviour quantitatively. We first extracted the energies of the local maxima (of sufficient prominence) of the peaks, shown in Supplementary Figure 14 for samples of six thicknesses. In contrast to Fig. 2c in the main text, the peak energies here are absolute rather than given relative to the band gap. This accentuates the presence of series of peaks (across all samples and over a range of temperatures) which each occur at similar energies and are thus plotted in the same colour.

The series of peaks are identified relative to the '11' series at roughly 1.9 eV, because this was the most reliably prominent peak across all data sets, with the most consistent behaviour. Peak series '12' and '13, though usually larger in amplitude than the reference series, were occasionally more complicated to clarify due to the possible presence of underlying twin peaks. The presence of peak series '12.5' for the 297 nm sample, a feature preserved across many temperatures distinct from peak series '13', is the most striking example of this. Peaks at energies higher than peak series '13' could not be reliably identified. More low-energy peaks were identifiable at lower temperatures. It is possible that they are present but not visible at higher temperatures due to the reduction in peak size and broadening of peak width with increasing temperature, as shown in Fig. 2b and 2e of the main text. The '0'-indexed series corresponds to the lowest energy discernible peak series at the lowest temperatures.

Peak widths

In order to obtain further quantitative information about the peak behaviour, Gaussian functions were fitted to the peaks in series '10', '11' and '12', which are the only series present at all temperatures in all samples. The full width at half maximum (FWHM) of the three Gaussian peaks averaged over all six samples at each temperature is plotted in Fig. 2b of the main text.

In Fig. 2b, this temperature-dependent broadening of the peaks is compared with that of the excitonic peak near the absorption onset. We quantitively assess these data with the function [26] $\Gamma(T) = \Gamma_0 + \Gamma_{\mathrm{LO}}$, where $\Gamma_{\mathrm{LO}} = \gamma_{\mathrm{LO}}/\left(e^{E_{\mathrm{LO}}/k_{\mathrm{B}}T} - 1\right)$, frequently used to describe the temperature-dependence of the absorption (or photoluminescence) linewidth. Here, Γ_0 is a temperature-independent inhomogeneous scattering term arising from disorder and imperfections, and homogeneous scattering from longitudinal optical (LO) phonons via the Fröhlich interaction contributes with charge-carrier coupling strength γ_{LO} for a representative LO phonon energy E_{LO} [26]. While acoustic phonons also contribute to homogeneous scattering, their contribution is sufficiently small for $FAPbI_3$ that it can be neglected, at least for the bulk excitonic peak [26].

Fits of $\Gamma(T)$ to the bulk excitonic linewidth data (solid red line in Fig. 2b, data near the phase transition excepted) describe the data well, and we find that Γ_0 =21 meV, E_{LO}= 19 meV and γ_{LO} = 57 meV, which are broadly consistent with previous reports for this material [26,28]. In contrast, the corresponding fit to the peak linewidths (solid blue line in Fig. 2b) yields values for $E_{\mathrm{LO}}$and γ_{LO} which are only 0.7 meV and 6 meV respectively. Such a substantially lower value of the coupling constant is indicative of considerably different origins of the broadening. We further note that the low returned value of E_{LO} suggests that the contribution to broadening from LO phonons may be sufficiently low for these confined states that acoustic phonons may now also need to be accounted for.

Peak areas

The central energy of the peak indexed ‘11’ plus the FWHM of the Gaussian peak fitted to it, was used as the upper limit of integration when obtaining the area under the peaks in each peak spectrum. The average of this area (as a percentage of the area under the total absorption spectrum in this range) over all six samples at each temperature is plotted in Fig. 2e of the main text.

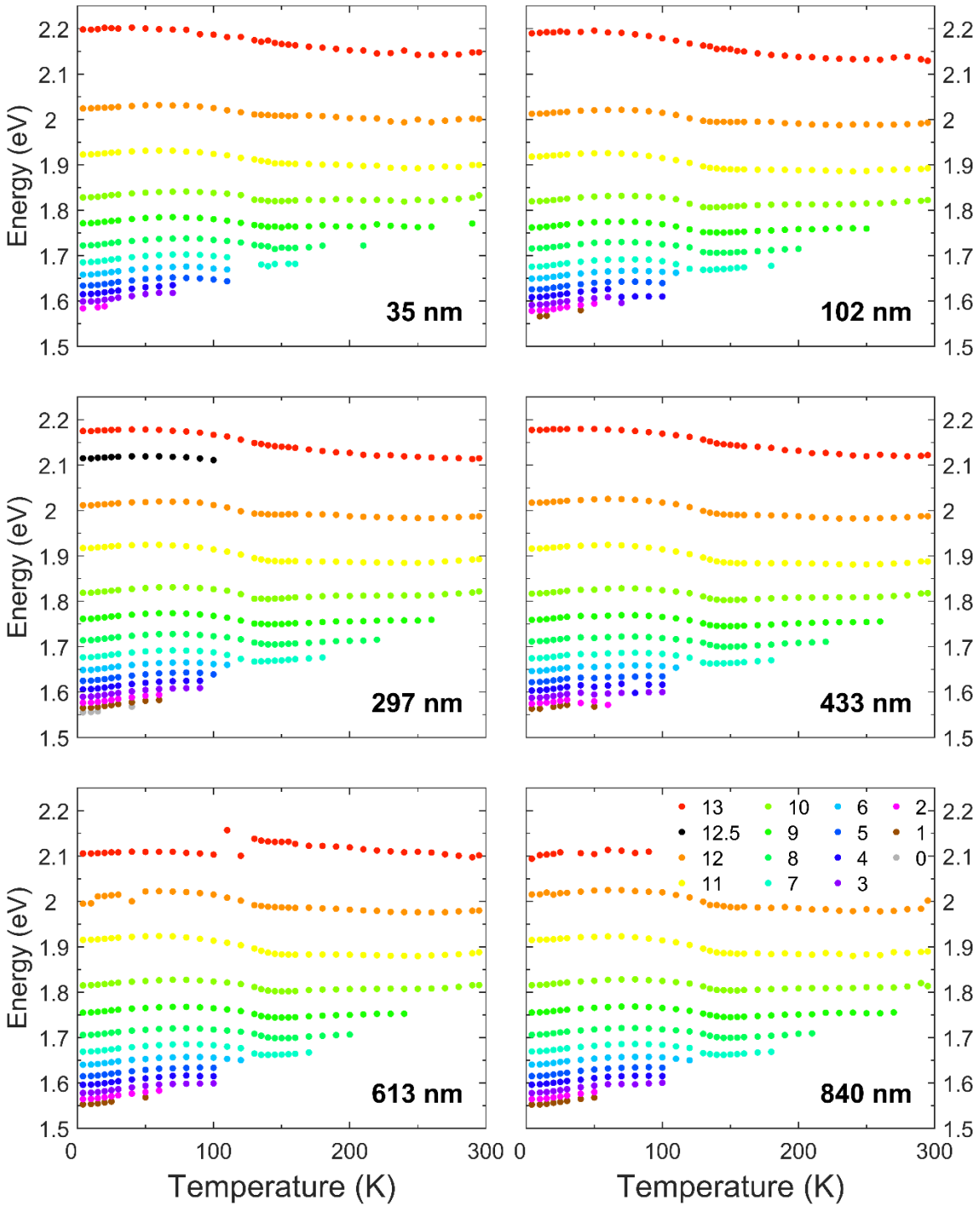

Supplementary Figure 14 | Temperature-dependent confinement peak energies. Energetic positions of the maxima of the absorption oscillation peaks of $FAPbI_3$ thin films as a function of temperature. The thicknesses of the films are indicated in the bottom-right corner of each panel. Peaks with similar energetic positions across different samples are assigned a particular index number, shown in the legend.

Supplementary Note 7: Quadratic Variation of Peak Energy

In Fig. 2d of the main text, the energy difference between the band gap and the oscillation peak energies (E_{peak} - E_g) of the 297-nm thick $FAPbI_3$ film at 4 K is plotted as a function of the peak index. As detailed in Supplementary Note 6, the peaks were identified relative to the '11' peak at roughly 0.40 eV above the band gap, which was the most prominent and consistent in behaviour across all temperatures and sample thicknesses. Data at 4 K were chosen because more peaks were visible at low temperatures, where they are larger and narrower. Within this data set, there were 15 peaks, including the peak indexed as '12.5' due to an apparent splitting in the '13' peak.

Intriguingly, Fig. 2d of the main text is suggestive of a quadratic relationship between the peak indices and E_{peak} - E_g. We now rationalise this in terms of confinement by first an infinite quantum well, then for the more involved case of confinement by a superlattice represented by a Krönig-Penney potential.

Infinite quantum well

We first consider the exemplary case of charge-carrier confinement within infinite potential barriers. While this model system is strictly speaking unphysical, it offers simple analytic solutions and provides a good approximation in particular for states deep inside a quantum well. For a system with a perfectly parabolic electronic density of states that has electronic confinement due to an infinite quantum well, the confinement energy of the n^{th} state varies as $E_n = \frac{h^2 n^2}{8m^* L^2}$, where m^* is the effective mass of the particle and L is the confinement length. If there is confinement in additional directions, then the confinement energies are simply additive [29], so that for a quantum dot the discrete energy levels are given by

$$E_{n_i,n_j,n_k} = \frac{h^2}{8m^* L^2}\left(n_i^2 + n_j^2 + n_k^2\right)$$

where n_i, n_j and n_k are the peak indices corresponding to the i, j, and k directions, whose confinement lengths are all assumed to be L. Thus, even when the number of confined dimensions is not known, there will still exist an inverse-square proportionality between the confinement energies and the confinement length.

Krönig-Penney superlattice

The quantum confinement that causes the oscillatory features observed in the absorption spectra is physically more likely to be derived from a periodic potential of finite height, deriving for example from relatively periodic ferroelectric walls or δ-phase insertions. One of the simplest such potentials is the Krönig-Penney potential, which is typically used to introduce the calculation of a simple electronic bandstructure containing band gaps within the nearly-free electron model. However, it is also possible to apply this approach to a superlattice of periodically-arranged quantum wells [30,31]. We therefore apply the Krönig-Penney model to our oscillation peak energies in order to show that they are consistent with such an origin.

We use a one-dimensional Krönig-Penney square well potential of infinite extent, $U(x)$, as shown in Supplementary Figure 15. The potential wells have width a, while the walls have width b and height U_0. By solving the Schrödinger equation within this potential, it is possible to show [30] that the dispersion relationship is

$$\cos(k[a+b]) = \frac{1-2\frac{E}{U_0}}{2\sqrt{\frac{E}{U_0}\left(1-\frac{E}{U_0}\right)}}\left\{\sin\left(\alpha_0 a\sqrt{\frac{E}{U_0}}\right)\sinh\left(\alpha_0 b\sqrt{1-\frac{E}{U_0}}\right)\right\} + \cos\left(\alpha_0 a\sqrt{\frac{E}{U_0}}\right)\cosh\left(\alpha_0 b\sqrt{1-\frac{E}{U_0}}\right)$$

where $\alpha_0 = \sqrt{\frac{2m^*U_0}{\hbar^2}}$, m^* is the effective mass of the electron, E is the energy and k is the wavenumber. The solutions to this dispersion relationship form a band structure as shown in Supplementary Figure 16.

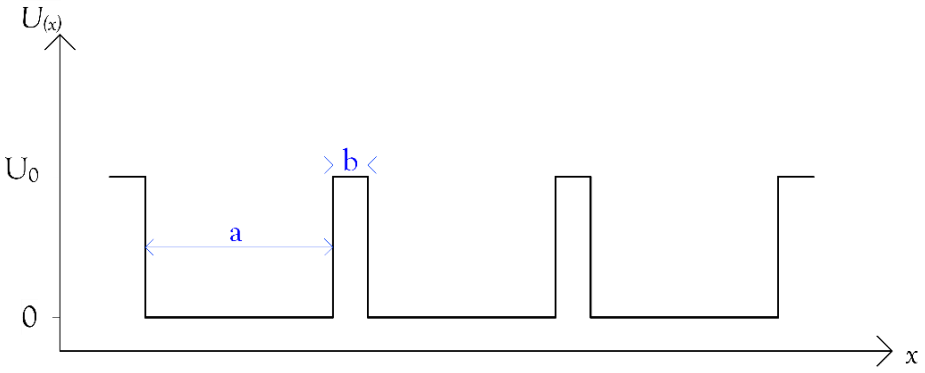

Supplementary Figure 15 | Krönig-Penney potential. Schematic plot of a section of the periodic square well potential, formed by wells of width a and walls of width b and a height of U_0.

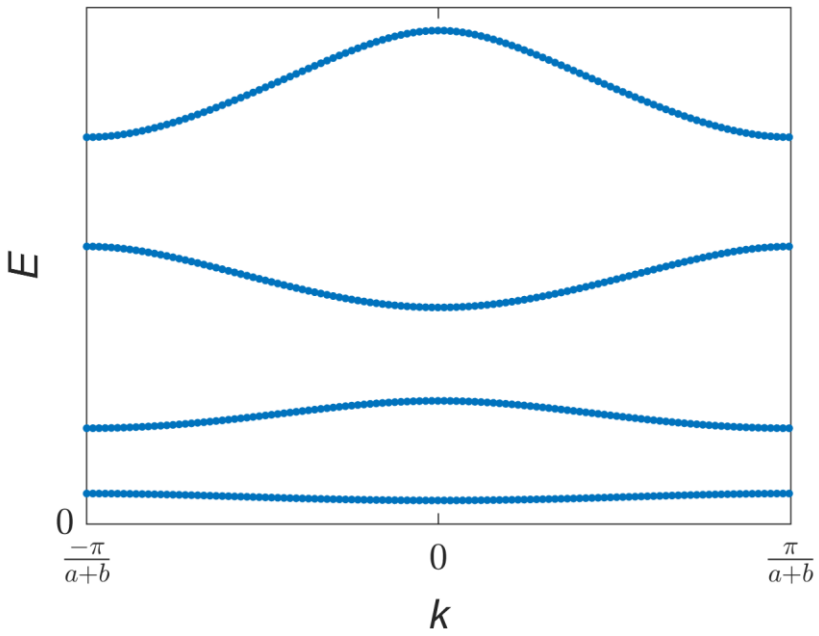

Supplementary Figure 16 | Krönig-Penney bands. Reduced-zone representation of the relationship between the energy (E) and wavenumber (k) of the states in the Krönig-Penney potential. Note that the states are arranged in bands which become broader with increasing energy.

Comparison with data

To test the data for the signature of quantum confinement, we first consider the simpler infinite well case. In Fig. 2d of the main text we therefore display a fit to the confinement peak energies with the generic expression

$$E_{\text{confinement}} = E_{\text{peak}} - E_{\text{g}} = A(n - n_0)^2 + B$$

where *A* is a constant of proportionality, *B* represents the shift of the lowest confinement energy from the band gap, and $n_0 = 0$ is the peak index at which the quadratic function starts (since this is the lowest-energy discernible peak). Due to the aforementioned unexplained splitting we excluded peaks above index '12' from the fit. The fit yields $B \approx 70$ meV, an energy shift of the ground state confinement energy from the bulk material band gap which may result from a different band gap within the confined region owing to lattice strain [17,32]. The quadratic function fits the data well, demonstrating that the energies of the peaks are supportive of the presence of quantum confinement within the infinite-well model. In reality, the applicability of the infinite quantum well model would require actual (finite) barrier heights in excess of several hundred millielectron volts, given that peak features are still observable this far above the band gap energy.

In Fig. 2d of the main text we also plot the midpoint energies of bands (equidistant between the maximum and minimum energy state in the band) obtained using the Krönig-Penney model with values of U_0 of 200 meV, a = 38nm, b =1 nm. With increasing band energy, the bands become broader in energy and their midpoint energies grow successively further apart, following a roughly quadratic dependence on peak index and thus also fitting the data well, when an energy shift of 75 meV is applied. The similarity of this dependence to the energies of the states in the infinite quantum well model confirms that the latter has merit as a means of conceptualising the confinement in $FAPbI_3$, despite its unphysical assumptions.

Indeed, the Krönig-Penney model demonstrates that potential barriers of finite height can still have a perturbing influence on unbound states ($E > U_0$). This is clear from Fig. 2d of the main text, in which confinement energies predicted by the Krönig-Penney model for potential barrier heights of 200 meV far exceed the values of this barrier height. Thus, the infinite quantum well model appears to be a surprisingly good approximation of the trends in confinement energies, even if these may exceed the barrier heights realistically present in the material.

Nonetheless, both approaches are somewhat simplistic because of the many assumptions involved. We particularly highlight two pertinent points. (1) The bands involved in the transitions are in fact not perfectly parabolic [22], and the complexities of which transitions are allowed in *k*-space are ignored. Since dependences on the variations of effective mass in different bands and directions are subsumed into *A*, further assumptions would be required in order to estimate a confinement lengthscale. The density functional theory (DFT) approach described in Supplementary Note 9 provides a much more sophisticated framework within which to make these assumptions and account for additional complexities arising from the actual bandstructure present in these systems. (2) The number of dimensions in which the charge-carrier motion is confined is unknown, and will have an effect on the confinement energies. Taken together, these two points mean that a reliable value of the confinement length scale cannot be accurately deduced from comparing such simple models to experimental data. The density functional theory approach detailed below attempts to overcome some of these issues.

Supplementary Note 8: Lattice Parameters and Peak Energies

The main panel of Fig. 2f in the main text shows the temperature dependence of $1/p^2$, where p is one of the reduced lattice parameters determined by Weber *et al.* from neutron diffraction measurements [27]. These are consistent with the measurements of Fabini *et al.*, who measured over a narrower temperature range [33].

Above 140 K (*β*-phase), Weber *et al.* modelled the structure of $FAPbI_3$ as tetragonal (*P4/mbm*), with lattice parameters *a* and *c*; by convention, the tetragonal unit cell has base dimensions *a* x *a*, and height *c*. By scaling these parameters, a tetragonal unit cell may be mapped onto a notional cubic unit cell in order to facilitate comparison between the lattice parameters, independently of the shape of the cell [34,35]. When $a < c$, the former is scaled upwards to $\sqrt{2}a$, but since the opposite is the case for $FAPbI_3$, Weber *et al.* instead use the reduced lattice parameter $a/\sqrt{2}$. Below 140 K (*γ*-phase), Weber *et al.* use a $1 \times 1 \times 6$ supercell expansion relative to the tetragonal structure assumed for the *β*-phase. In this, the FA cation rotates in increments along the long *c*-axis, which is consequently scaled to $c/6$ when plotted as a reduced lattice parameter.

The plots of $1/p^2$ in Fig. 2f in the main text show similar temperature trends to those of $E_{\mathrm{peak}}(T) - E_{\mathrm{g}}(T)$ in Fig. 2c in the main text. Therefore, the inset to this figure compares the reduced lattice parameters with the oscillation peak energies in order to establish whether they are related in a way consistent with quantum confinement. To seek out such a parallel, we therefore consider the case of charge-carrier confinement within infinite potential barriers. As detailed in Supplementary Note 7, this simple potential is able to reasonably reproduce the confinement effects resulting from the more realistic cause of a superlattice.

As detailed in Supplementary Note 7, if the energy difference between the oscillation peak energy at a given index (E_{peak}) and the band gap (E_{g}) is a confinement energy ($E_{\mathrm{confinement}}$), with the associated confinement length proportional to the lattice parameter, then we would expect a relationship of the form

$$E_{\mathrm{confinement}}(T) = E_{\mathrm{peak}}(T) - E_{\mathrm{g}}(T) = \frac{Q}{p(T)^2} + B$$

where *B* represents any offset of the confinement energy from the band gap, which may, for example, result from the materials being subject to strain-related energy shifts within the confined domain. Here, *Q* is a proportionality coefficient which includes the effective mass of the charge carriers and the scaling factor between *p* and the actual confinement length. If we assume that *Q* and *B* are independent of temperature, then we can express *Q* as

$$Q = \frac{E_{\mathrm{confinement}}(T) - E_{\mathrm{confinement}}(T_0)}{1/p(T)^2 - 1/p(T_0)^2}$$

where T_0 is a given temperature. The model is self-consistent if *Q* for the measured data is constant with respect to *T*. In the inset of Fig. 2f, *Q* is plotted for peak series 12 of the 297 nm sample, with T_0 = 120 K for the *γ*-phase and T_0 = 295 K for the *β*-phase, for both the cases of *p* derived from *a* and *c*. Different T_0 values are used for each phase to account for the abrupt shift in both $E_{\mathrm{confinement}}$ and $p(T)$ at the phase transition (the range 120 – 160 K is therefore not plotted).

Q appears constant in the *γ*-phase and slightly less so in the *β*-phase. This is supportive of the view that the oscillation peak energies result from quantum confinement, with the length scale linearly related to the lattice parameter. As the lattice expands with increasing temperature, so too does the

length of the confining potential responsible for the absorption peaks. Deviations from the temperature-independence of Q may result from temperature dependence within B or the effective charge-carrier mass; the latter has been measured to vary slightly between 2 K and 150 K [36].

Supplementary Note 9: First-Principles Calculations

This section outlines the calculation of more realistic confinement energies and length scales for charge-carriers inside a simple particle-in-a-box system presented by $FAPbI_3$, taking account of the actual bandstructure of $FAPbI_3$ through first-principles calculations. In order to calculate the absorption spectrum [37] of $FAPbI_3$, it is first necessary to simulate its electronic band structure. For an organic-inorganic hybrid perovskite like $FAPbI_3$, this is non-trivial and so we make certain simplifying assumptions. In order to simplify the structure, we choose to replace the formamidinium (FA) cation by adding one electron per formula unit (in place of that usually donated by the FA in becoming a cation). This substitution allows us to study the Pb-I contribution to the optical properties without introducing artefacts due to the chosen FA placement and/or orientation; this is justified because there is no direct contribution of the A-site cation to the band edges of the perovskite [36].

We model this abstract structure using a simple cubic lattice, as has been experimentally observed [38] for α-$FAPbI_3$, which has lattice parameter a =6.362 Å at room temperature. As a result of the uncertainty surrounding the nature of the low-temperature γ-phase, which may be disordered [27] and thus present computational difficulties, we retain the cubic lattice for simulations at 0 K. Due to the well-known limitations of density functional theory (DFT), the band gap of the cubic phase of $FAPbI_3$ is underestimated, and the bands appear significantly distorted; thus, the band dispersions and the absorption spectrum are initially inaccurate compared to the known electronic band structure of $FAPbI_3$ [39]. Correcting this presents an opportunity to make the lattice consistent with the temperature: we slightly increase the lattice constant by 4 % to a =6.608 Å, and rigidly shift the band gap by 1.23 eV so as to match the experimentally observed value of 1.5 eV at 4 K [1].

The resulting electronic band structure is shown in Supplementary Figure 17, focused on the region around the direct band gap as these are the only bands involved in absorption at the energies we are concerned with.

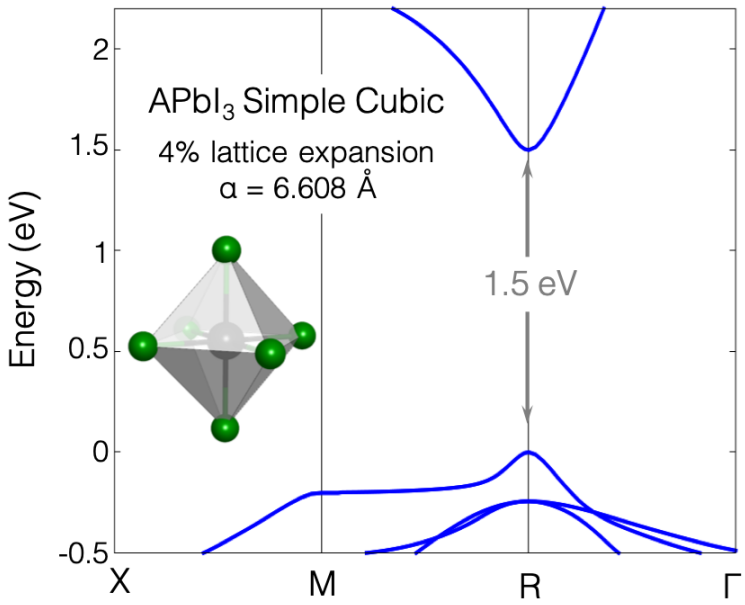

Supplementary Figure 17 | Electronic band structure of $APbI_3$. DFT simulation of the electronic band structure of $FAPbI_3$ at the energies near the direct gap, using a cubic structure with the FA

cation replaced by an electron per formula unit and the A-site empty. The structure is shown on the left (green = I, black = Pb). The lattice parameter a is 6.608 Å.

We move on to model the effects of confinement on the optical properties. To do so we perform a series of calculations of the absorption coefficient employing discrete k-point grids. Assuming a three-dimensional quantum confinement in the simple particle-in-a-box picture, the size of the k-point grid is related to the confinement size as follows:

$$k = \frac{n\pi}{L} \Rightarrow \frac{2\pi}{a} = \frac{n\pi}{L} \Rightarrow L = \frac{na}{2}$$

with *L* the confinement size, *n* the k-grid subdivision, and a the lattice constant. For example, in the case of the cubic lattice of $FAPbI_3$, a k-point grid of size 10x10x10 (10^3) corresponds to a spatial confinement of 3.3 nm, 20^3 is 6.6 nm, 30^3 is 9.9 nm, 40^3 is 13.2 nm, and 50^3 is 16.5 nm. The absorption coefficient is then computed at the independent particle level. Using this approach, we calculated the absorption coefficients shown in Fig. 3b in the main text. As discussed below, we applied an energetic broadening of 10 meV to the calculated spectra. As expected, we observe oscillations of the spectrum with energy separations corresponding to differences between the quantized valence and conduction band states. These oscillations become closer in energy for larger confinement sizes. By comparison with the experimental spectrum, we can see that the measured oscillations are most compatible with quantum confinement effects with a characteristic length of around 13 nm or 17 nm.

In Supplementary Figure 18, we show the calculated absorption coefficient for a confinement size of 10nm, calculated with different values of energy broadening, ranging from 1 meV to 40 meV. In Fig. 3b of the main text, we chose a smearing of 10 meV in order to optimise comparability with the measured spectrum; this value allowed a slight merging of adjacent peaks, without losing information on peak location.

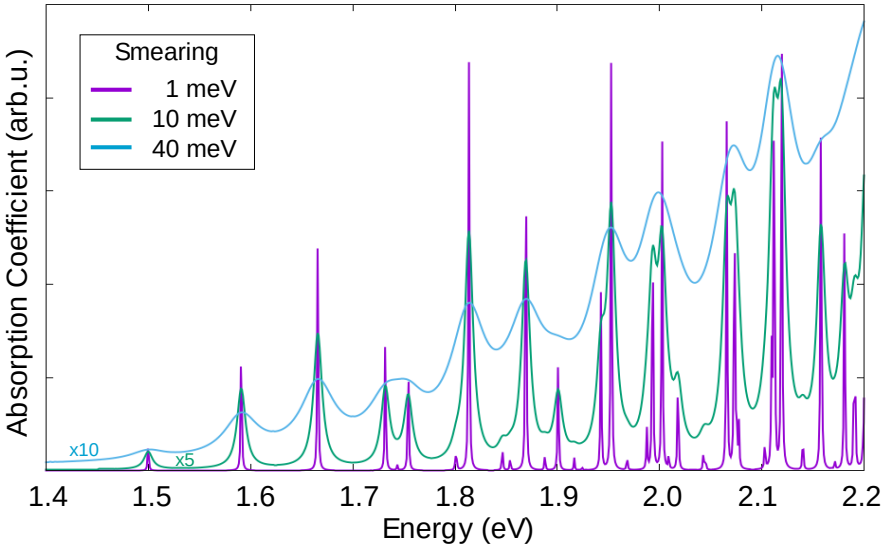

Supplementary Figure 18 | Effect of smearing on simulated absorption. Absorption coefficient for a confinement length of 10 nm (30^3 k-grid) employing different smearing values. The spectra are scaled vertically with respect to each other by the factors indicated in the corresponding colours.

In addition, we modelled the scenario in which the structure is confined along one direction only, corresponding to confinement in only one dimension (a quantum well). To do so, we calculated the absorption coefficient using a k-point grid of 50x50x20, which corresponds to a quantum-confined structure of size 17 nm x 17nm x 6 nm and compared it with the case of 17 nm confinement along all three directions. Supplementary Figure 19 shows the calculated absorption coefficient spectra for the two cases, using a smearing of 1 meV. The features thus obtained are very similar in the two scenarios, which makes it difficult to ascertain whether the measured absorption features are attributable to confinement in only one or the full three dimensions.

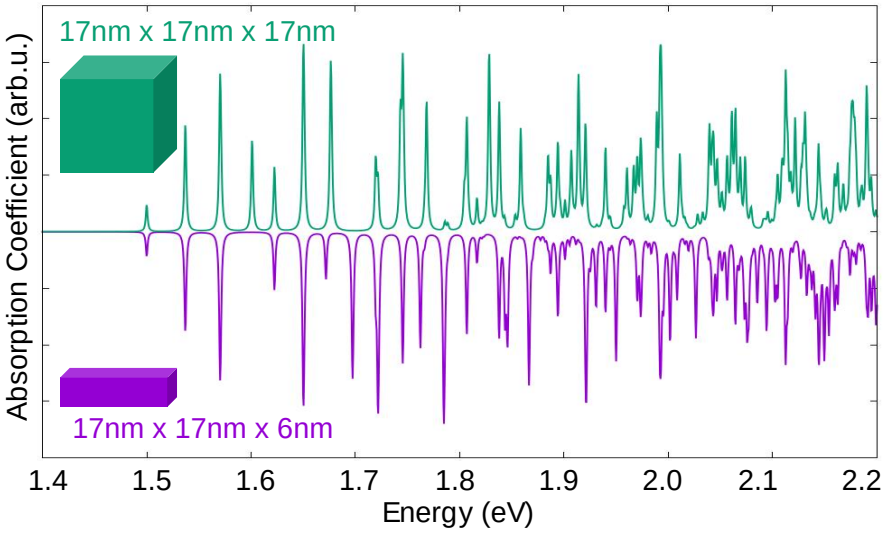

Supplementary Figure 19 | 3D vs 1D confinement. Absorption coefficient for a confinement along three-dimensions (green) of 17nm x 17nm x 17nm and (purple) along two-dimensions 17nm x 17nm and one-dimension of 6nm.

All calculations in this manuscript were performed using the Quantum-ESPRESSO suite [40]. For calculating the electronic structure of $FAPbI_3$ we employed fully relativistic norm-conserving Perdew–Burke–Ernzerhof (PBE) [41] pseudopotentials [42] with a kinetic energy cut-off of 100 Ry and a k-point grid of 20x20x20. All calculations include spin-orbit coupling [43]. For the calculations of the optical absorption coefficient at the independent-particle level we used the YAMBO code [44] for Fig. 3b of the man text and Supplementary Figure 19, whereas for Supplementary Figure 18 the Quantum-ESPRESSO code was used [40].

Supplementary Note 10: 3D Density of states for a 1D superlattice

As discussed in Supplementary Note 7, the particle-in-a-box model represents an effective but ultimately unphysical means of considering confinement within $FAPbI_3$. There, it was also shown that a more physical periodic, finite potential in one dimension can nonetheless influence the energetic distribution of 1D electronic states at energies above the height of the potential barriers. Here, we generalise this result to a three-dimensional free electron gas under a one-dimensional periodic square-like potential. As with a Krönig-Penney potential, this potential represents a 1D superlattice.

By numerically solving the central equation [45]

$$E_{\mathrm{k}}\, c(G) + \sum_{G'} V(G' - G) c(G') = \epsilon\, c(G)$$

for a nearly-free electron with *k*-points in all three directions, we are able to model the electronic states at the conduction or valence band of $FAPbI_3$, using an effective electron mass of $m^* = 0.1\, m_{\mathrm{e}}$. Here, ϵ are the energy eigenvalues, E_{k} is the kinetic energy, G is any reciprocal lattice vector and $c(G)$ are the coefficients for the vectors. V is the periodic potential shown in Supplementary Figure 20: a square-like wave potential with amplitude V_0, analogous to a Krönig-Penney potential (as shown in Supplementary Figure 15) with $V_0 = U_0/2$. Numerical solution of the central equation followed the procedure given by Kittel [45], but generalised to three dimensions. We used an energy cut off for the sphere of the g-vectors of 1 eV. The free electron expands up to 600 nm, which corresponds to a total sum of g-vectors employed for the calculations of 15.515.

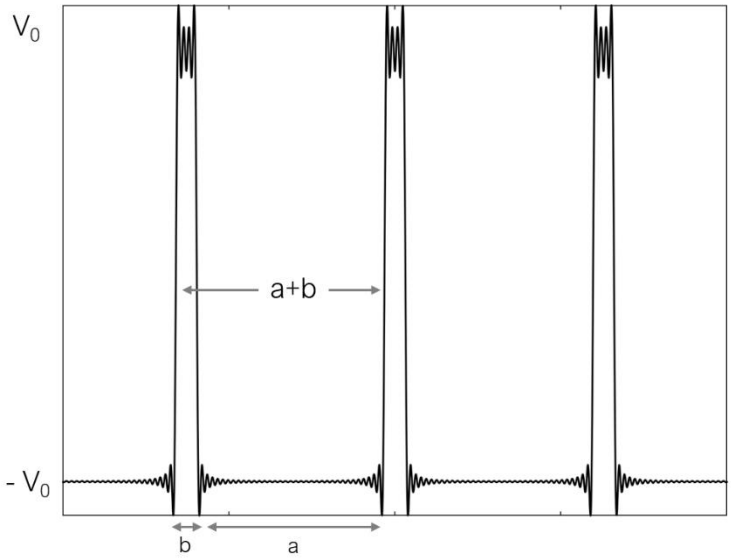

Supplementary Figure 20 | Square-like wave potential. The periodic potential that is acting on the free electron, with wells of width *a* and walls of width *b*. The potential is square-like, with an amplitude of V_0.

Supplementary Figure 21 shows the effects on the electronic density of states (DOS) of varying the amplitude of the potential, while Fig. 3c of the main text shows the effects of varying the period. Note that the general square-root functional form of the DOS is a consequence of it arising from electrons

in a 3D structure, with the effect of confinement felt along only one dimension and appearing as an undulation of the 3D DOS. Since the states are discrete, the DOS plots are smeared using a Gaussian broadening function with an adaptive smearing factor of 1 meV to 100 meV within the energy range of -0.1 eV to 1 eV, and shifted to have their first eigenvalue at 0 eV.

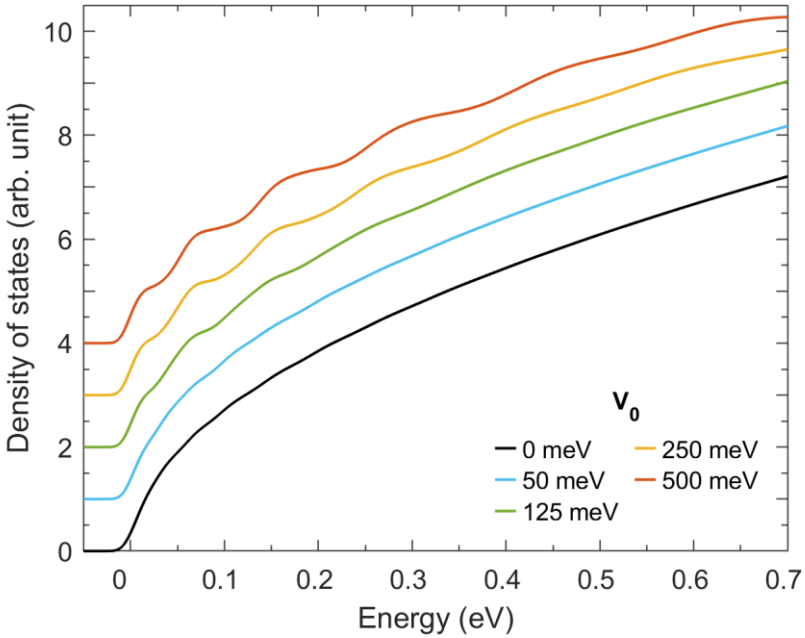

Supplementary Figure 21 | 3D Density of states (DOS) for a 1D square-like wave potential. The wall width *b* is set to one-tenth of the period (*a* + *b*) of the potential. The effect on the DOS of varying the amplitude, V_0, is shown for a fixed period of 15 nm. The black line shows the free electron case (with no periodic potential).

For the effective mass of $m^* = 0.1m_e$ and the wall width *b* set to one tenth of the period (*a* + *b*) of the potential, we find that a 1D square-wave potential as shown in Fig. 3c of the main text can induce oscillation-like features in the DOS that are on a comparable energy scale to those we observe in the absorption spectra of $FAPbI_3$. When the amplitude of the potential increases, the features become more pronounced, as shown in Supplementary Figure 21. This model therefore shows clearly that a simple 1D Krönig-Penney potential can induce oscillation-like or peak features in the DOS of a 'nearly free' electron in 3D, even above height of the potential. Applying such a potential is a generalisation of the confinement by infinite barriers used in the first-principles calculations detailed in Supplementary Note 9.

Supplementary Note 11: Thinnest Film (10 nm)

The $FAPbI_3$ thin films reported in Fig. 2 of the main text range in thickness from 35 nm to 840 nm. We also measured a thinner film, of nominal thickness 10 nm, as determined by the time the substrate was exposed to the PbI_2 and FAI vapours (see Supplementary Note 12). Due to its low thickness, this film was the most fragile. Water infiltration into the perovskite [4] resulted in its conversion to the hexagonal non-perovskite *δ*-phase due to exposure to humidity [2] during transport to, and measurement in, the x-ray diffractometer. This was in contrast to measurements in the FTIR spectrometer, during which the samples were kept in a helium atmosphere.

Although the thickness of this film was measured using an atomic force microscope (AFM) to be 26 ± 5 nm, there are reasons to doubt the accuracy of this value. In Supplementary Figure 22a, the absorption coefficient obtained using a thickness of 10 nm for this film is compared to that of the 35 nm film. Although the absorption coefficients for the two films do not match exactly in magnitude, the agreement would be far worse if the thinner film data were scaled down by a factor of 2.6. For $MAPbI_3$, the absorption coefficient is expected to be independent of thickness even down to films 2 nm thick [32], and we expect similar for $FAPbI_3$. Therefore, we consider the 10 nm nominal thickness to be more accurate than that measured by AFM.

Given that vapour-deposited films form islands of material during the initial part of their growth, the film thickness measured using AFM may not represent the majority of the sample which lies between such islands [32], while degradation during the AFM measurement in air is also likely to have occurred. The absorption spectra for the 10 nm film were measured in an inert He atmosphere, therefore such degradation was absent.

As shown in Fig. 3a of the main text and Supplementary Figure 22b, the confinement peaks are less evident in the 10 nm sample than the 35 nm one (for which they are similar in strength to that for the other, thicker films; see Supplementary Figure 10) at 4 K, and are not visible at room temperature. This suggests that the film thickness of around 10 nm is close to the lower limit at which the peaks can appear; thus for thinner films the quantum confinement responsible for the peaks would not be able to arise as its characteristic length scale would not fit within the film. Allowing for some uncertainty in the actual thickness of the film, this observation supports our DFT calculations which estimate the confinement length responsible for the features to be approximately 13 nm.

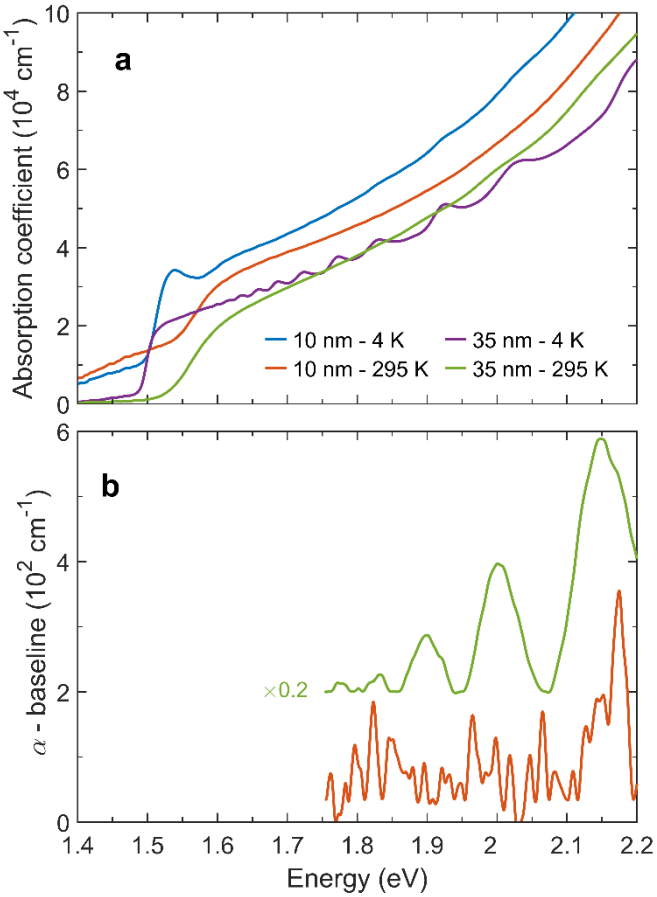

Supplementary Figure 22 | Absorption coefficient and peak features of 10-nm thick $FAPbI_3$ film. a) Absorption spectra and **b)** absorption peak features of a 10-nm thick $FAPbI_3$ film, at 4 K (blue) and 295 K (red), compared with the corresponding data for a 35-nm thick film. The peaks for the 35-nm thick film are scaled vertically by a factor of 0.2 and offset vertically by 2×10^2 cm^{-1}.

Supplementary Note 12: Measurement of the Film Thicknesses

For films deposited as described in Supplementary Note 1, the nominal film thicknesses were determined by monitoring the rate of PbI_2 and FAI vapour deposition using a quartz crystal microbalance (QCM) and measuring the length of time for which the substrate was exposed to the vapours. The thicknesses of the thicker films were also measured with a DEKTAK profiler, while for the two thinnest films an Asylum Research MFP-3D atomic force microscope was used instead. In both cases a razor blade was used to scratch away the film in a section of the sample to then measure the height difference between the film and the scratched region. For each sample multiple measurements were taken and averaged.

Nominal thickness (nm)	Measured thickness (nm)
1000	840 ± 10
500	613 ± 4
380	433 ± 3
250	297 ± 2
100	102 ± 1
30	35 ± 5
10	*(26 ± 5)*

Supplementary Table 1 | Nominal and measured thicknesses of $FAPbI_3$ films. The mean and standard errors are shown for the measured thickness of each film. The measured thickness for the thinnest film is in brackets and *italic* because it is at odds with the optical thickness of the film and is not considered representative of the film as a whole.

Supplementary Note 13: Ferroelectric Domain Width

Lines and Glass [46] derive the following expression for the mean domain width of a ferroelectric domain by considering the balance between contributions to the free energy of the crystal, which is reduced by ferroelectric ordering but is increased by energy associated with the domain walls (due to unaligned dipoles) and domain volume (the energy of the depolarization field which acts against ferroelectric polarisation):

$$d = \left(\frac{\sigma t}{\varepsilon^* P_0^2} \right)^{1/2}$$

which is known as Kittel's law [47]. Here, d is the domain width, σ is the energy per unit area of the domain wall, ε^* is a constant depending on the dielectric constants of the ferroelectric and P_0 is the polarisation at the centre of a domain. For a single crystal, t represents the crystal thickness, but in polycrystalline thin films such as those used in this study, the grain thickness is a more appropriate interpretation since the film may contain more than one layer of grains. Indeed, whereas solution-processed thin films have been produced with grains whose thickness is equivalent to the film thickness of hundreds on nanometres [48], in dual-source evaporated perovskites (as used here) the grains are usually smaller [49,50].

As calculated by Frost *et al.* [37], the lattice electronic polarisation (analogous to P_0) is smaller in $MAPbI_3$ than $FAPbI_3$ (38 vs 63 μC cm^{-2}). Conversely, $MAPbI_3$ has the larger nearest-neighbour dipole interaction energy (4.6 vs 0.03 kJ mol^{-1}), which contributes to σ. The static and high-frequency dielectric constants of the two materials are very similar [51]. Based on these parameter values, for grains of equal thickness we would expect ferroelectric domains in $FAPbI_3$ to be around twenty times smaller than those in $MAPbI_3$. The reported measurements of polar domains ranging between 90 and 300 nm in width in $MAPbI_3$ [52,53] were taken on single crystals and solution-processed films, so it is possible that smaller grain thicknesses in our vapour-deposited films could also contribute to smaller ferroelectric domain widths.

Supplementary Note 14: Exciton Bohr Radius

The exciton Bohr radius can be used as an indicator of whether quantum confinement effects are to be expected at a given confinement lengthscale. It is given by [22]

$$a_{\mathrm{B}} = a_{\mathrm{H}}\epsilon_r \frac{m_{\mathrm{e}}}{\mu}$$

where a_{H} is the hydrogenic Bohr radius (5.29×10^{-2} nm), ϵ_{r} is the dielectric constant of the material and μ is reduced effective mass of the electron-hole system. The dielectric constant can be related to the exciton binding energy, E_{b}, and the Rydberg constant, R_{H} (13.6 eV) by

$$\epsilon_{\mathrm{r}} = \sqrt{\frac{R_{\mathrm{H}}}{E_{\mathrm{b}}}\frac{\mu}{m_{\mathrm{e}}}}$$

Using $\mu \approx 0.09 m_{\mathrm{e}}$ as measured for $FAPbI_3$ by Galkowski *et al.* [36], and taking $E_{\mathrm{b}} \approx 2 - 5$ meV for the temperature range 295 K – 4 K (see Supplementary Figure 12), we estimate that $a_{\mathrm{B}} \approx 10 - 15$ nm over this range of temperatures. Such a value is consistent with quantum confinement effects occurring, given our estimated domain width of 10-20 nm.

Another rough indicator of the plausibility of confinement effects is the de Broglie wavelength, λ_{dB}, of a particle, especially towards room temperature when $k_{\mathrm{B}}T$ exceeds the exciton binding energy. Using

$$\lambda_{dB} = \frac{h}{\sqrt{m^* k_{\mathrm{B}} T}}$$

with an effective single particle charge-carrier mass of $m^* \approx 0.2 m_{\mathrm{e}}$, we obtain a de Broglie wavelength of at room temperature of $\lambda_{\mathrm{dB}} \approx 24$ nm. This is still consistent with (exceeding) our estimated confinement length.

Supplementary Note 15: High Temperature Absorption

In order to ascertain the temperature at which the absorption peak features disappeared, it was necessary to measure at temperatures above room temperature. We carried out high-temperature experiments on two films, of thicknesses 613 nm and 297 nm. Since the gas-exchange helium cryostat (Oxford Instruments, OptistatCF2) used in the previous absorption measurements is not suitable at such high temperatures, we instead mounted the samples in a cold-finger cryostat (Oxford Instruments, MicrostatHe), with the same settings on the FTIR as detailed in Supplementary Note 3 but without the capacity to measure reflectance.

The results from the first high-temperature experiment, using a 613-nm thick film, are shown in panels a and b of Supplementary Figure 23. The oscillations observable in the transmittances in panel a were extracted as peaks (panel b) by adapting the baseline fitting procedure described in Supplementary Note 4. The sample was first cooled to 4 K, then heated up to 500 K. Above room temperature, the oscillations continue to become less prominent. and the oscillations disappear at 380 K. After having been heated up to 500 K, this film appeared yellow on return to room temperature, indicating permanent degradation of the $FAPbI_3$ to PbI_2.

Panels c and d depict the transmittances and peak features respectively from the second high-temperature experiment, which was based on a 297-nm thick film. This sample was also cooled to 4 K, before this time being heated up to only 380 K. The extinction of the oscillations at 380 K was again observed. However, this time the features reappeared upon cooling back from 380 K to 295 K, and the sample did not appear yellow, demonstrating that the process is reversible, provided the maximum temperature reached is not too high.

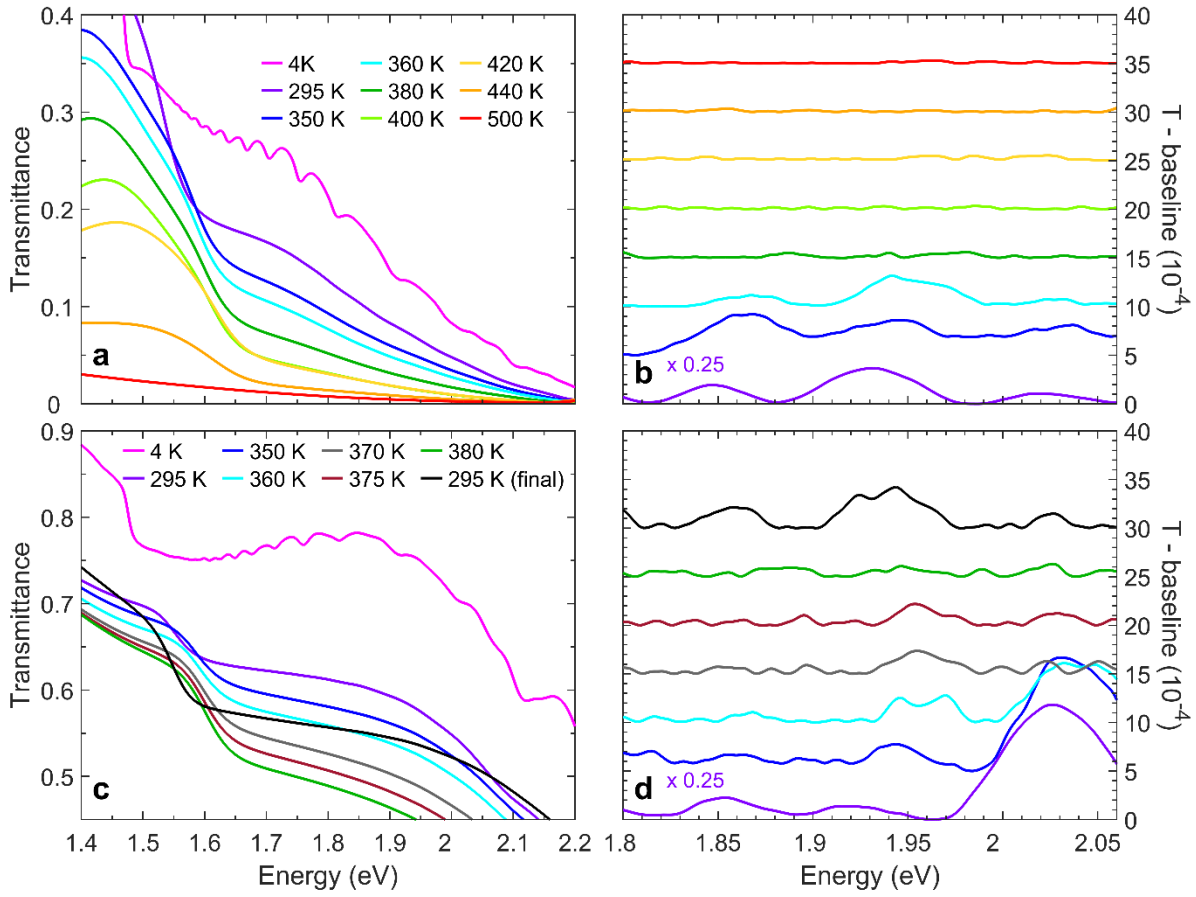

Supplementary Figure 23 | High temperature transmittance and peak features. a) Transmittance spectra and **b)** transmission peak features of a 613 nm $FAPbI_3$ film heated from 4 K to 500 K. The features disappear at 380 K (dark green). **c)** and **d)** show the corresponding data for a 297 nm thick film heated from 4 K to 380 K (dark green), at which temperature the peak features again disappeared. However, the peaks are again present in the data (black lines) collected after the sample was subsequently cooled down to 295 K. For both samples, successive peak feature measurements are shown vertically offset from each other by 5×10^{-4}, while the peaks of the initial data at 295 K are scaled vertically by a factor of 0.25.

Supplementary References

1. Davies, C. L. *et al.* Impact of the organic cation on the optoelectronic properties of formamidinium lead triiodide. *J. Phys. Chem. Lett.* **9**, 4502–4511 (2018).

2. Borchert, J. *et al.* Large-area, highly uniform evaporated formamidinium lead triiodide thin films for solar cells. *ACS Energy Lett.* **2**, 2799–2804 (2017).

3. West, A. R. *Solid State Chemistry and its Applications*. (Wiley, 2014).

4. Müller, C. *et al.* Water infiltration in methylammonium lead iodide perovskite: fast and inconspicuous. *Chem. Mater.* **27**, 7835–7841 (2015).

5. Patel, J. B., Milot, R. L., Wright, A. D., Herz, L. M. & Johnston, M. B. Formation dynamics of $CH_3NH_3PbI_3$ perovskite following two-step layer deposition. *J. Phys. Chem. Lett.* **7**, 96–102 (2016).

6. Rühle, S. Tabulated values of the Shockley – Queisser limit for single junction solar cells. *Sol. Energy* **130**, 139–147 (2016).

7. Wehrenfennig, C. Ultrafast spectroscopy of charge separation, transport and recombination processes in functional materials for thin-film photovoltaics. (University of Oxford, 2014).

8. Stoumpos, C., Malliakas, C. & Kanatzidis, M. Semiconducting tin and lead iodide perovskites with organic cations: phase transitions, high mobilities, and near-infrared photoluminescent properties. *Inorg. Chem.* **52**, 9019–9038 (2013).

9. Koh, T. M. *et al.* Formamidinium-containing metal-halide: an alternative material for near-IR absorption perovskite solar cells. *J. Phys. Chem. C* **118**, 16458–16462 (2014).

10. Ma, F. *et al.* Stable α/δ phase junction of formamidinium lead iodide perovskites for enhanced near-infrared emission. *Chem. Sci.* **8**, 800–805 (2016).

11. Li, Y. *et al.* Formamidinium-based lead halide perovskites: structure, properties, and fabrication methodologies. *Small Methods* **2**, 1700387 (2018).

12. Grätzel, M. The rise of highly efficient and stable perovskite solar cells. *Acc. Chem. Res.* **50**, 487–491 (2017).

13. Han, Q. *et al.* Single crystal formamidinium lead iodide ($FAPbI_3$): insight into the structural, optical, and electrical properties. *Adv. Mater.* **28**, 2253–2258 (2016).

14. Wu, J., Walukiewicz, W. & Haller, E. E. Band structure of highly mismatched semiconductor alloys: coherent potential approximation. *Phys. Rev. B* **65**, 233210 (2002).

15. Yu, P. Y. & Cardona, M. *Fundamentals of Semiconductors*. (Springer-Verlag, 2010).

16. Fang, H. *et al.* Quantum of optical absorption in two-dimensional semiconductors. *PNAS* **110**, 11688–11691 (2013).

17. Eperon, G. E. *et al.* Formamidinium lead trihalide: a broadly tunable perovskite for efficient planar heterojunction solar cells. *Energy Environ. Sci.* **7**, 982–988 (2014).

18. Lv, S. *et al.* One-step, solution-processed formamidinium lead trihalide ($FAPbI_{(3-x)}Cl_x$) for mesoscopic perovskite-polymer solar cells. *Phys. Chem. Chem. Phys.* **16**, 19206–19211 (2014).

19. Pang, S., Hu, H., Zhang, J., Lv, S. & Yu, Y. $NH_2CH{=}NH_2PbI_3$: An alternative organolead iodide perovskite sensitizer for mesoscopic solar cells. *Chem. Mater.* **26**, 1485–1491 (2014).

20. Zhang, Y. *et al.* Trash into treasure: δ-$FAPbI_3$ polymorph stabilized $MAPbI_3$ perovskite with power conversion efficiency beyond 21%. *Adv. Mater.* **30**, 1707143 (2018).

21. Wei, Q., Zi, W., Yang, Z. & Yang, D. Photoelectric performance and stability comparison of $MAPbI_3$ and $FAPbI_3$ perovskite solar cells. *Sol. Energy* **174**, 933–939 (2018).

22. Davies, C. L. *et al.* Bimolecular recombination in methylammonium lead triiodide perovskite is an inverse absorption process. *Nat. Commun.* **9**, 293 (2018).

23. Elliott, R. J. Intensity of optical absorption by excitions. *Phys. Rev.* **108**, 1384–1389 (1957).

24. Wright, A. D. *et al.* Band-tail recombination in hybrid lead iodide perovskite. *Adv. Funct. Mater.* **27**, 1700860 (2017).

25. Varshni, Y. P. Temperature dependence of the energy gap in semiconductors. *Physica* **34**, 149–154 (1967).

26. Wright, A. D. *et al.* Electron–phonon coupling in hybrid lead halide perovskites. *Nat. Commun.* **7**, 11755 (2016).

27. Weber, O. J. *et al.* Phase behavior and polymorphism of formamidinium lead iodide. *Chem. Mater.* **30**, 3768–3778 (2018).

28. Fang, H.-H. *et al.* Photoexcitation dynamics in solution-processed formamidinium lead iodide perovskite thin films for solar cell applications. *Light Sci. Appl* **5**, e16056 (2016).

29. Klingshirn, C. F. *Semiconductor Optics*. (Springer Berlin Heidelberg, 2012).

30. Razeghi, M. *Fundamentals of Solid State Engineering*. (Springer, 2019).

31. Carpena, P., Gasparian, V. & Ortuño, M. Number of bound states of a Kronig-Penney finite-periodic superlattice. *Eur. Phys. J. B* **8**, 635–641 (1999).

32. Parrott, E. S. *et al.* Growth modes and quantum confinement in ultrathin vapour-deposited $MAPbI_3$ films. *Nanoscale* **11**, 14276–14284 (2019).

33. Fabini, D. H. *et al.* Reentrant structural and optical properties and large positive thermal expansion in perovskite formamidinium lead iodide. *Angew. Chem. Int. Ed.* **55**, 15392–15396 (2016).

34. Brivio, F. *et al.* Lattice dynamics and vibrational spectra of the orthorhombic, tetragonal and cubic phases of methylammonium lead iodide. *Phys. Rev. B* **92**, 144308 (2015).

35. Zhu, H. *et al.* Charge transfer drives anomalous phase transition in ceria. *Nat. Commun.* **9**, 5063 (2018).

36. Galkowski, K. *et al.* Determination of the exciton binding energy and effective masses for methylammonium and formamidinium lead tri-halide perovskite semiconductors. *Energy Environ. Sci.* **9**, 962–970 (2016).

37. Frost, J. J. M. J. *et al.* Atomistic origins of high-performance in hybrid halide perovskite solar cells. *Nano Lett.* **14**, 2584–2590 (2014).

38. Weller, M. T., Weber, O. J., Frost, J. M. & Walsh, A. Cubic perovskite structure of black formamidinium lead iodide, α-$[HC(NH_2)_2]PbI_3$, at 298 K. *J. Phys. Chem. Lett.* **6**, 3209–3212 (2015).

39. Chen, T. *et al.* Origin of long lifetime of band-edge charge carriers in organic–inorganic lead iodide perovskites. *PNAS* **114**, 7519–7524 (2017).

40. Giannozzi, P. *et al.* QUANTUM ESPRESSO: a modular and open-source software project for quantum simulations of materials. *J. Phys. Condens. Matter.* **21**, 395502 (2009).

41. Perdew, J. P., Burke, K. & Ernzerhof, M. Generalized gradient approximation made simple. *Phys. Rev. Lett.* **77**, 3865–3868 (1996).

42. Hamann, D. R. Optimized norm-conserving Vanderbilt pseudopotentials. *Phys. Rev. B* **88**, 085117 (2013).

43. Even, J., Pedesseau, L., Jancu, J.-M. & Katan, C. Importance of spin-orbit coupling in hybrid organic/inorganic perovskites for photovoltaic applications. *J. Phys. Chem. Lett.* **4**, 2999–3005 (2013).

44. Marini, A., Hogan, C., Grüning, M. & Varsano, D. yambo: An ab initio tool for excited state calculations. *Comp. Phys. Commun.* **180**, 1392–1403 (2009).

45. Kittel, C. *Introduction to Solid State Physics*. (John Wiley & Sons, 2004).

46. Lines, M. E. & Glass, A. M. *Principles and Applications of Ferroelectrics and Related Materials*. (Oxford University Press, 1977).

47. Kittel, C. Theory of the structure of ferromagnetic domains in films and small particles. *Phys. Rev.* **70**, 965–971 (1946).

48. Chiang, C. H., Nazeeruddin, M. K., Grätzel, M. & Wu, C. G. The synergistic effect of H_2O and DMF towards stable and 20% efficiency inverted perovskite solar cells. *Energy Environ. Sci.* **10**, 808–817 (2017).

49. Ball, J. M. *et al.* Dual-source coevaporation of low-bandgap $FA_{1-x}Cs_xSn_{1-y}Pb_yI_3$ perovskites for photovoltaics. *ACS Energy Lett.* **4**, 2748–2756 (2019).

50. Ávila, J., Momblona, C., Boix, P. P., Sessolo, M. & Bolink, H. J. Vapor-deposited perovskites: the route to high-performance solar cell production? *Joule* **1**, 431–442 (2017).

51. Umari, P., Mosconi, E. & De Angelis, F. Infrared dielectric screening determines the low exciton binding energy of metal-halide perovskites. *J. Phys. Chem. Lett.* **9**, 620–627 (2018).

52. Röhm, H. *et al.* Ferroelectric properties of perovskite thin films and their implications for solar energy conversion. *Adv. Mater.* **31**, 1806661 (2019).

53. Wilson, J. N., Frost, J. M., Wallace, S. K. & Walsh, A. Dielectric and ferroic properties of metal halide perovskites. *APL Mater.* **7**, 010901 (2019).